



# Electron-rich/poor reaction sites enable ultrafast confining Fenton-like processes in facet-engineered BiOI membranes for water purification

Wei Qu<sup>a</sup>, Cheng Chen<sup>a</sup>, Zhuoyun Tang<sup>a</sup>, Dehua Xia<sup>a,b,\*</sup>, Dingren Ma<sup>a</sup>, Yajing Huang<sup>a</sup>, Qiyu Lian<sup>a</sup>, Chun He<sup>a,b,\*</sup>, Dong Shu<sup>c</sup>, Bin Han<sup>d</sup>

<sup>a</sup> School of Environmental Science and Engineering, Sun Yat-sen University, Guangzhou 510275, China

<sup>b</sup> Guangdong Provincial Key Laboratory of Environmental Pollution Control and Remediation Technology, Guangzhou 510275, China

<sup>c</sup> Key Lab of Technology on Electrochemical Energy Storage and Power Generation in Guangdong Universities, School of Chemistry and Environment, South China Normal University, Guangzhou 510006, China

<sup>d</sup> Key Laboratory for City Cluster Environmental Safety and Green Development of the Ministry of Education, Institute of Environmental and Ecological Engineering, Guangdong University of Technology, Guangzhou 510006, China

## ARTICLE INFO

### Keywords:

Facet-engineered BiOI membranes  
Electron-rich/poor centers  
Confinement  
Oxygen vacancies  
Water purification

## ABSTRACT

Heterogeneous Fenton-reaction accomplishes the destruction of pollutants via the oxidation of hydroxyl radicals during water purification. Herein, two facet-engineered (control of different exposed crystal planes) BiOI nanocatalysts (BI-001 and BI-110) as the dual-reaction-center catalysts were loaded on the polyvinylidene fluoride membrane, remarkably accelerating the occurrence of Fenton-reaction and leading to the enhanced degradation of the pollutants in complex water matrices. The degradation efficiency of paracetamol by BI-110 membrane (~96.0%) was significantly higher than that of BI-001 membrane (~26.1%) in catalytic activity. The electron paramagnetic resonance tests and theoretical calculations proved that BI-110 possesses more oxygen vacancies, which acts as the electron-rich sites to trigger the Fenton-reaction. Correspondingly, the pollutants were adsorbed on the electron-poor Bi<sup>3+</sup> sites and donate electrons during the degradation process. This study provides a candidate strategy to break the limitations of Fenton reaction advanced oxidation processes for water purification using the tunable facet-engineered BiOI membrane.

## 1. Introduction

The Fenton/Fenton-like reaction is currently one of the widest applied advanced oxidation processes (AOPs) [1,2], in which hydrogen peroxide (H<sub>2</sub>O<sub>2</sub>) is activated by metal ions (e.g., Fe<sup>2+</sup>) or other heterogeneous catalysts to generate hydroxyl radicals (•OH, E<sub>0</sub> = 2.80 V/NHE) contributing to the oxidative degradation of pollutants [3,4]. In the homogeneous Fenton reaction, the inseparability of the active ingredients and the secondary pollution caused by the leaching of metal ions during the reaction are the two main problems. Generally, these limitations can be avoided by using heterogeneous catalysts, such as metals, metal oxides and metal-supported catalysts [5,6]. However, heterogeneous Fenton catalysts still have some shortcomings, such as the poor catalytic performance under neutral conditions, poor reusability and low utilization efficiency of H<sub>2</sub>O<sub>2</sub> because the activation of H<sub>2</sub>O<sub>2</sub> is attributed to the redox reactions of surficial metal sites [7,8]. However, the cycles of redox reactions result in the leaching of the

soluble metal ions into the solution, thus deteriorating the catalytic activity and stability of the catalyst. Besides, the reduction of metal species is the rate-limiting step in the whole reaction process, which further leads to poor catalytic performance [9]. Therefore, the key point to solve these problems is to optimize the mechanism of H<sub>2</sub>O<sub>2</sub> activation by the cycles of redox reactions.

It is possible to selectively decompose H<sub>2</sub>O<sub>2</sub> by constructing the Fenton-like catalytic system with the dual-reaction centers (i.e., electron-rich center and electron-poor center). Explicitly, the electron-rich center can activate H<sub>2</sub>O<sub>2</sub> to generate •OH by undergoing a reduction reaction and the electron-poor center can adsorb other electronic sacrificial substances (electron donors), such as organics and their intermediate products. In this way, it can not only improve the utilization rate of H<sub>2</sub>O<sub>2</sub>, but also achieve the rapid degradation of pollutants [10, 11]. Lyu et al. demonstrated that the oxygen species introduced by molecular doping on will simultaneously cause the increase of the electron density around the doped oxygen atom. Consequently, the

\* Corresponding authors at: School of Environmental Science and Engineering, Sun Yat-sen University, Guangzhou 510275, China.

E-mail addresses: [xiadehua3@mail.sysu.edu.cn](mailto:xiadehua3@mail.sysu.edu.cn) (D. Xia), [hechun@mail.sysu.edu.cn](mailto:hechun@mail.sysu.edu.cn) (C. He).

non-uniform distribution of electrons adjacent to the large  $\pi$  bond induce the countless of electron-rich oxygen centers and electron-poor carbon centers, further forming the dual reaction-centers [12]. Cao et al. reported a novel catalyst by the surface modification of reduced copper species, in which the combination of reductive metal species ( $\text{Cu}^0/\text{Cu}^+$ ) with polymers promotes the anomalous phase transfer of electrons ( $\text{Cu} \rightarrow \text{O} \leftarrow \text{C}(\pi)$ ), resulting in polar-enhanced O-electron-rich reactive centers and  $\text{C}(\pi)$ -electron-poor reactive centers [13]. However, the construction of the cation- $\pi$  structure often needs complex synthetic

processes. The  $\pi$  structures of carbon-rings are often easily destroyed by the free radicals generated from Fenton reactions. Therefore, constructing strong polar reaction sites on the surface of the catalyst to create more efficient and convenient means could be an effective approach for the enhanced Fenton/Fenton-like water treatment technology. Recently, many investigations have demonstrated that the oxygen vacancies (OVs) are effective in promoting Fenton-like reactions by the metal oxide-based catalysts [14]. Li et al. observed the abundant defect structures across the different crystal planes in the  $\text{BiOCl}$ , such as

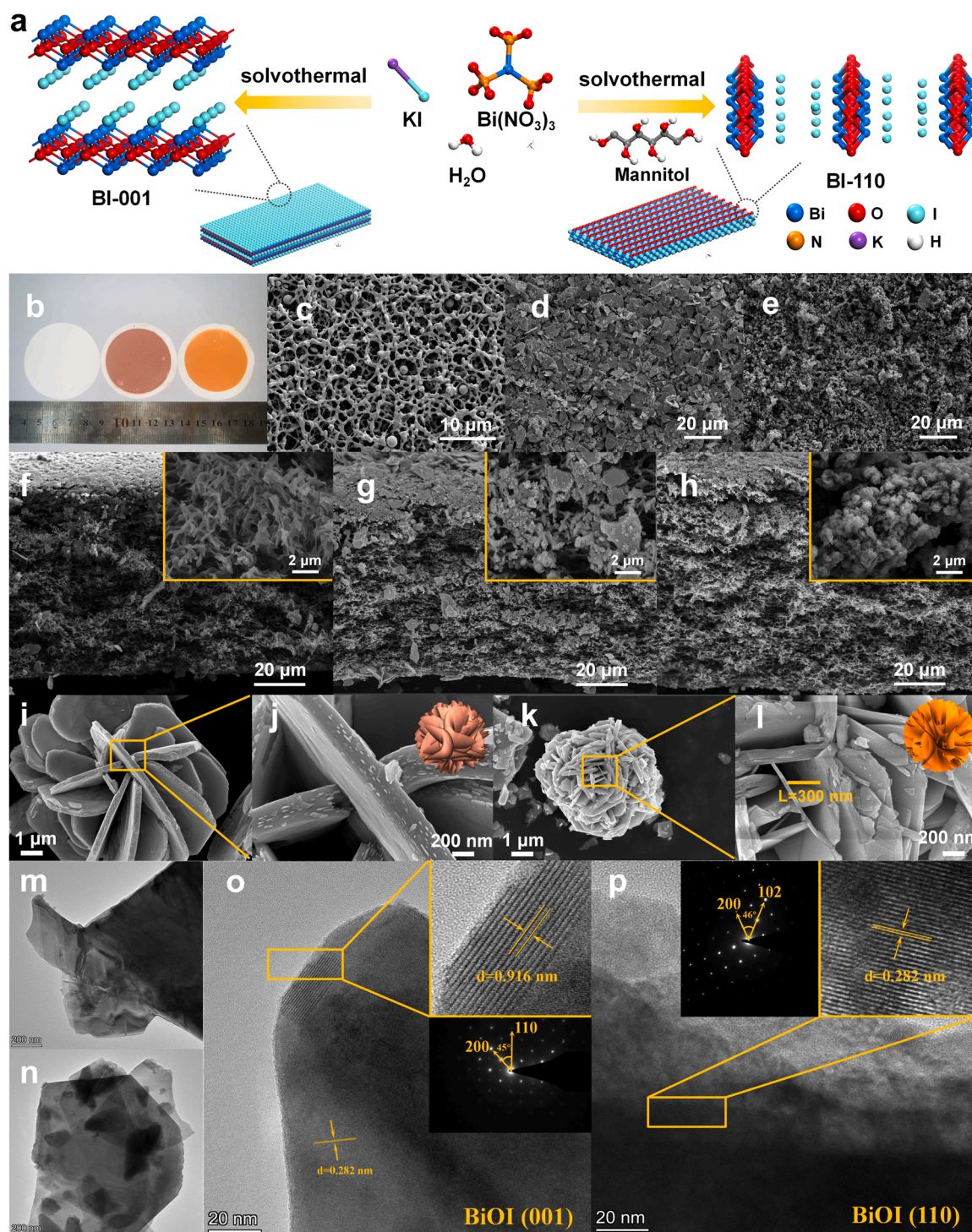


**Fig. 1.** (a) Schematic illustration of preparation of BI-001 and BI-110; (b) Photographs of the bare PVDF membrane (left), BI-001 membrane (middle) and BI-110 membrane (right); SEM image of the top surface and cross-sections of PVDF membrane (c, f), BI-001 membrane (d, g) and BI-110 membrane (e, h); SEM morphology of BI-001 (i, j) and BI-110 (k, l) membranes; TEM and HR-TEM of BI-001 (m, o) and BI-110 (n, p) membranes.



lattice distortion and missing atoms, and thus constructed a low-toxicity non-transition metal oxide BiOCl with adjustable OV concentration to make the transition from Fenton-inert to Fenton-active [15]. Although the electron-gain/loss cycles of OVs have not been specifically revealed, these studies lead us to believe that OVs play a key role on the electronic modulation and electron transfer on surface of the catalyst.

Meanwhile, the short lifetime of radicals is another challenge in Fenton-like systems. Notably, a spatial confinement system can reduce the molecular diffusion distance and maximize the utilization of short-lived free radicals [16,17], such as assembling catalysts into a membrane. In this way, the mass transfer between  $\text{H}_2\text{O}_2$  and the activator will be significantly accelerated, thereby enhancing the activation of  $\text{H}_2\text{O}_2$  to generate a higher concentration of hydroxyl radicals. Herein, facet-engineered BiOI (i.e., BI-110 and BI-001) nanocatalysts were synthesized and coated onto polyvinylidene fluoride membranes for the first time, performing the near-completed destruction of pollutants by water through single-pass treatment at a permeate water flux equivalent to common UF processes (Fig. S1). Moreover, the BiOI membrane shows a great stability, which is available for the long-term reclaimed water purification. This study will broaden the application range of the constructed catalyst through facet-engineering membrane-confined AOP treatment systems.

## 2. Materials and methods

### 2.1. Chemicals and materials

All chemicals for the preparation of experimental materials in this study were of analytical grade and used without further purification. The details are given in Text S1.

### 2.2. Characterizations

The measurements of X-ray diffraction (XRD), scanning electron microscopy (SEM), energy-dispersive X-ray spectroscopy (EDS), transmission electron microscopy (TEM), high-resolution TEM (HR-TEM), X-ray photoelectron spectroscopy (XPS), electron paramagnetic resonance (EPR), total organic carbon (TOC), and  $\text{N}_2$  adsorption-desorption isotherms were in this study, and the details are described in Text S2.

### 2.3. Preparation of BiOI membranes

BiOI nanocatalysts with exposed (001) and (110) facets, denoted BI-001 and BI-110, respectively, were prepared by a hydrolysis method (Fig. 1a and Text S3). The reference samples were prepared by annealing BI-001 and BI-110, named BI-001-H and BI-110-H, respectively. BiOI nanocatalysts were coated onto layered PVDF membranes by the vacuum filtration method. A certain amount (0–25 mg) of BI-001/Bi-110 nanocatalysts and BI-110 nanocatalysts were filtered using a hydrophilic PVDF membrane (0.22  $\mu\text{m}$  pore size, 50 mm diameter, 70  $\mu\text{m}$  thickness). The BI-001 and BI-110 membranes were obtained after vacuum drying at 70  $^\circ\text{C}$  for 10 h. The as-prepared membranes were labeled as “BI-001/Bi-110 membrane” with the molecular weight cutoff reduced to 500 kDa (Text S4 for details).

### 2.4. Membrane performance test

The catalytic performance of the prepared membrane was evaluated by activating  $\text{H}_2\text{O}_2$  to degrade various emerging phenolic contaminants (paracetamol, bisphenol A and 4-chlorophenol) and non-phenolic contaminants (ibuprofen) (Tables S1 and Fig. S2). Herein, the BiOI membrane was applied in an actual flow-through device to explore the pollutant removal performance (Fig. S3). The layered membrane was sealed tightly by O-ring rubber bands to avoid water leakage in a filter cup, in which all the subsequent permeation experiments were carried out. The introduce of pressurized gas pushes the solution of paracetamol

(PCM) and  $\text{H}_2\text{O}_2$  to pass through the membrane. The stock solution in a water tank ([dosing container] $_v \approx 15\text{ L}$ , [stirring tank] $_v \approx 100\text{ mL}$ ), i.e., the background water containing  $\text{H}_2\text{O}_2$  (2 mM) and a model compound (e.g., PCM, 10–500  $\text{mg L}^{-1}$ ), was fed into the membrane module at prescribed flow rates under different transmembrane pressures controlled by a nitrogen tank. For the long-term performance test, the stock solution was replenished every 24 h.

### 2.5. Analytical methods

The measurement of PCM concentration and the detection of intermediate products are described in Text S5. The determination of the surface-to-volume ratio (SVR) is shown in Text S6. The calculation method of water flux and membrane porosity is shown in Text S7. The concentration of  $\text{H}_2\text{O}_2$  is determined by the ammonium metavanadate method [18], and the detailed calculation steps are given in Text S8 and S9. The experimental method of microorganism inactivation is shown in Text S10. Electrochemical analysis methods are listed in Text S11. The methods applied to identify the active species are shown in Text S12. The methods of reusability and activity evaluation are detailed in Text S13. The specific DFT calculation method of Fukui function is shown in Text S14.

## 3. Results and discussion

### 3.1. Fabrication and characterization of facet-engineered BiOI membrane

The color of the PVDF membrane changed from white to deep red and brownish yellow after the loading of BI-001 and BI-110, respectively (Fig. 1b). Compared with the original PVDF membrane (Fig. 1c), of the nanocatalysts are evenly dispersed on the surface of the PVDF membranes. The SEM images show that both of the surface views of BI-001 and BI-110 membranes look dense without obvious pores at a magnification of 1000 times (Fig. 1d, e). As expected, the thickness of the membrane increased from  $70 \pm 1.5\text{ }\mu\text{m}$  to  $74 \pm 2.5\text{ }\mu\text{m}$  after the addition of BiOI nanocatalysts. The cross-sectional views of catalytic membranes are featured with typical asymmetric structures composed of finger-like macro voids, are similar to that of the blank membrane (Fig. 1f, g, h). That is, the addition of BiOI nanocatalysts does not affect the formation of the dense skin layer and finger-like pore structure of PVDF membrane. In the magnified views of cross-sections of BiOI membranes, the nanocatalysts could be clearly observed. The roughly reticular morphology enhanced the surface roughness of the membrane, which could be beneficial for water permeability owing to the higher specific surface area available for water molecules to pass through [19]. As shown in Fig. S4, the contact angles decreased slightly when BiOI nanocatalysts were blended in PVDF membrane, and the contact angle of BI-110 decreased dramatically with the increase of the contact time. This result suggested that the introduction of BiOI nanocatalysts noticeably improves the hydrophilicity of PVDF membranes, which could improve the permeability and antifouling behavior of the membranes [20].

The SEM images of BI-001 membrane (Fig. 1i, j) reveal that its morphology is a hierarchical structure consisting of nanosheets, whereas the thickness of BI-110 ( $\sim 30\text{ nm}$ ) is much thinner than BI-001 ( $\sim 200\text{ nm}$ ) (Fig. 1k, l). The TEM, HR-TEM images and selected area electron diffraction pattern (SAED) further confirm the facets on the as-prepared BI-110 and BI-001 membranes. The angle (Fig. 1m, o) between the (110) plane and the (200) plane is  $45^\circ$ , and the lattice fringe is 0.916 nm, corresponding to the (001) plane of BI-001. In contrast, the atomic plane (Fig. 1n, p) with a lattice spacing of 0.282 nm verifies the exposed (110) plane of as-synthesized BI-110. In addition, the mapping of Bi, O and I demonstrates the uniform dispersion of these elements in BI-110 and BI-001 membranes as shown in Fig. S5.

The XRD patterns of BI-001 and BI-110 membranes are consistent with the standard card diffraction peaks of the tetragonal BiOI

(JCPDS10-0045) (Fig. 2a), indicating that the pure phase of BiOI was successfully synthesized [21]. Notably, the analysis of the ratios of  $I_{\{001\}}/I_{\{102\}}$  (1.09) and  $I_{\{110\}}/I_{\{102\}}$  (0.52) shows that BI-001 and BI-110 mainly grow towards [001] and [110] direction (Fig. S6), respectively. The full XPS spectra of the BI-001 and BI-110 membranes, shown in Fig. 2b, reveals the presence of Bi, O and I elements with high purity. The binding energies of Bi 4f are 159.2 and 164.5 eV, corresponding to the Bi 4f 7/2 and Bi 4f 5/2 orbitals of trivalent Bi, respectively. In the O1s region, the main peak at 529.9 eV is attributed to the Bi-O bond in BiOI layered structure  $(\text{BiO})_2^{2+}$  plate [22], and the other peak at 531.5 eV is attributed to the oxygen species adsorbed on OVs (Fig. 2c) [23–26]. The I 3d spectrum of the samples contains two peaks at 619.1 eV (I 3d3/2) and 630.5 eV (I 3d5/2), indicating that iodine exists in the form of  $\Gamma^-$  (Fig. S7).

The Raman spectra of BI-001 and BI-110 membranes, shown in Fig. 2d, are similar with obvious peaks at 150.5 and 85.7  $\text{cm}^{-1}$ , corresponding to the stretching vibration models of the internal Bi-I bond of  $A_{1g}$  and the internal Bi-I bond of  $E_g$  in BiOI [27,28], respectively. Compared with BI-001, the intensity of the peak in BI-110 obviously decreased (Fig. 2d), which could be due to the presence of more OVs leading to a decrease in crystallinity [29]. The detection of unpaired electrons by EPR can further directly reflect the OVs present on the catalyst surface. As shown in Fig. 2e, the EPR signal of BI-001 membrane is weaker than that of BI-110 membrane ( $g = 2.005$ ), indicating that the BI-110 possesses more OVs over BI-001. For the BI-110 membrane, the EPR signal of unpaired electrons is very strong, demonstrating that the regulation of the crystal plane leads to the formation of OVs on the BiOI surface and changes the local electronic environment of OVs [30]. In addition, with a 0.15 g loading of BI-110 and a specific surface area of 2.76  $\text{m}^2 \text{g}^{-1}$  (Fig. S8), the ratio of the available catalyst specific surface area to the inner volume of BI-110 membrane (0.11  $\text{cm}^3$ ) was estimated to be  $3.76 \times 10^6 \text{ m}^2 \text{m}^{-3}$  (Text S6).

### 3.2. Catalytic performance of facet-engineered BiOI membrane

The combination of BiOI nanocatalysts and PVDF membrane makes it easy to be integrated into a membrane-based water purification system (Fig. 3a, b). However, sufficient catalytic sites are what we expect,

but too much loading of BiOI may cause partial pore blockage on the membrane surface. Hence, evaluating the effects of the loading amount of BiOI on the filtration performance of modified membranes is of great significance in practical application. Fig. 3c shows the variation of pure water flux and membrane porosity of different samples. With the increase of the loading amount of BI-110 from 0 to 25 mg, the porosity of these membranes reduced from 87.4% to 82.1%, resulting in a pure water flux reduction from 591.8  $\text{L m}^{-2} \text{h}^{-1}$  (initial pure water flux) to 28.1  $\text{L m}^{-2} \text{h}^{-1}$ . Using as-synthesized BI-110 membrane, however, we observed the complete removal of PCM at membrane water fluxes up to  $\sim 120 \text{ L m}^{-2} \text{h}^{-1}$  ([catalysts loading] = 10 mg) (Fig. 3d). This translates to the complete destruction of PCM molecules at a retention time down to about 10 s in the membrane pores (Fig. S9). Considering the relationship between water flux and porosity, we selected a BI-110 membrane with a loading of 10 mg ( $\sim 120 \text{ L m}^{-2} \text{h}^{-1}$ ) for the subsequent tests (Fig. S10 and Text S7).

BiOI membranes have no catalytic activity in the absence of  $\text{H}_2\text{O}_2$ , and the removal efficiency of PCM on the BI-110 and BI-001 is about 5.5% and 4.2%, respectively, which demonstrates that BiOI membranes show a negligible adsorption capacity towards PCM (Fig. S11). Although the permeability of membrane decreases at high water flow rate, PCM can be effectively removed by the BI-110 membrane/ $\text{H}_2\text{O}_2$  and the removal efficiency can reach 96.0% within 60 s (Fig. 3d). The superior removal performance could be attributed to the highly exposed active surface and crystal planes in the lamellar structure of BiOI, generating a large number of  $\bullet\text{OH}$  by the rapid decomposition of  $\text{H}_2\text{O}_2$  (Fig. S12). In contrast, the removal efficiency ( $\sim 66.1\%$ ) of PCM in the presence of BI-110 nanocatalysts alone is much lower (Fig. 3e). Noteworthy, PCM was removed faster in the BI-110 membrane/ $\text{H}_2\text{O}_2$  system than that in the static batch experiments (Fig. S13). The catalytic degradation efficiency of PCM using various catalysts, listed in Table S2, clearly reveals that the BI-110 membrane exhibits great catalytic performance.

Fick's Law states that the flux flows from a high-concentration area to a low-concentration area, and its magnitude is proportional to the concentration gradient (spatial derivative). In the nanometer-scale spacing, the concentration gradient (perpendicular to the flow direction) has the potential to promote the transfer of target pollutants and  $\text{H}_2\text{O}_2$  from the flow center to the boundary. The rapid mass transfer

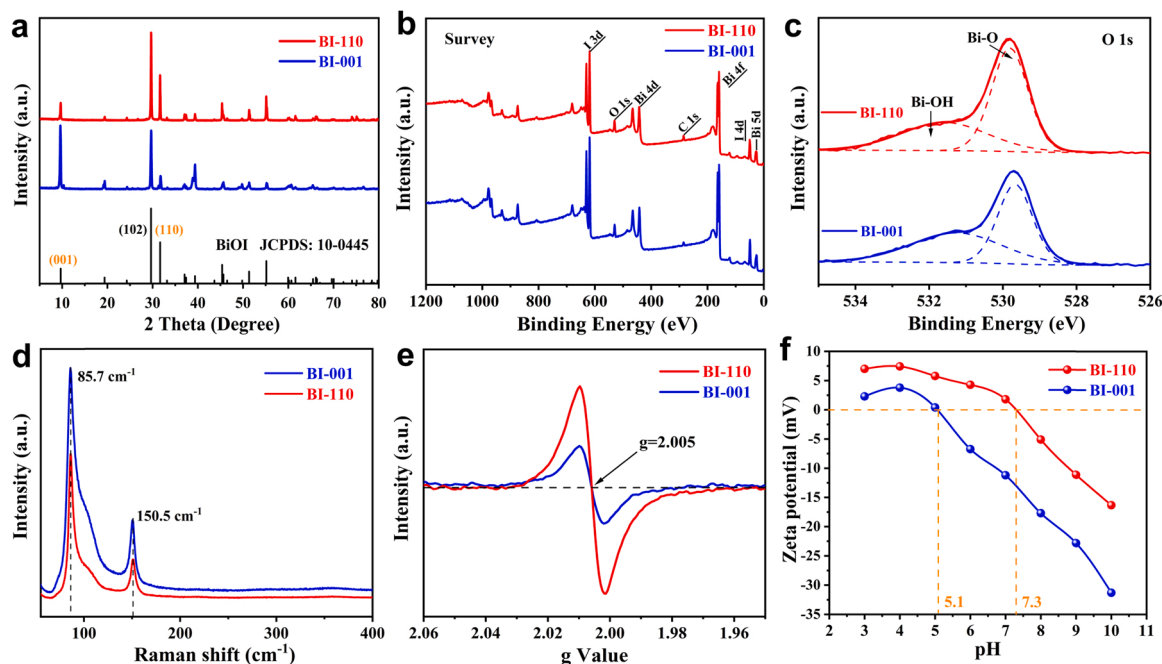
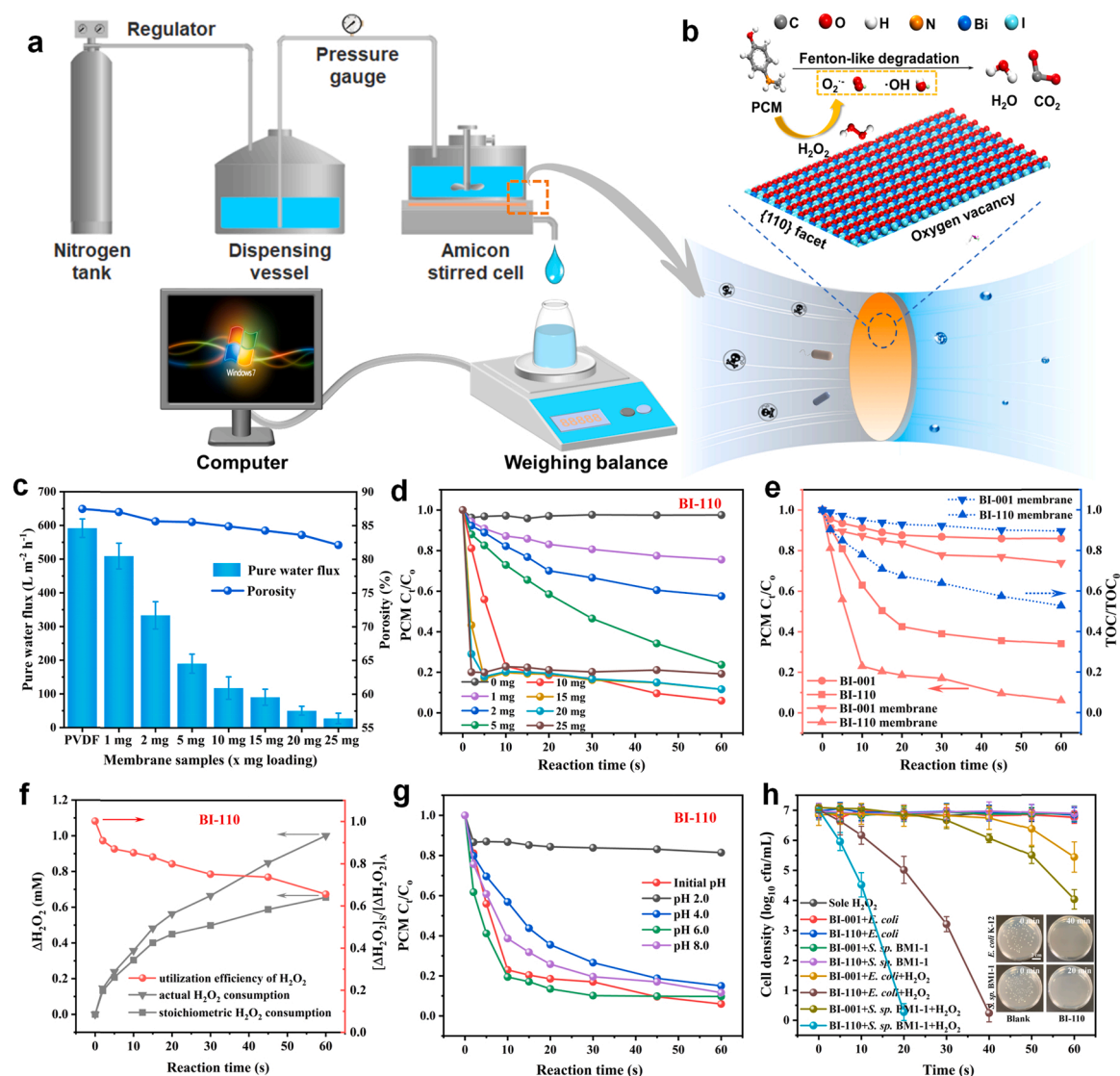


Fig. 2. (a) XRD patterns of BiOI membranes; (b) XPS total survey spectra and (c) high-resolution spectra of O 1s; (d) Raman pattern, (e) EPR analysis and (f) Zeta potential of BiOI membranes.





**Fig. 3.** (a) Schematic illustration of the setup for flow-through membrane reaction experiments; (b) Schematic diagram of BI-110 membrane structure; (c) Pure water flux and porosity of different BI-110 samples at room temperature; (d) Effect of catalyst concentration during PCM degradation in BiOI membranes; (e) Catalytic performance of BiOI nanocatalysts and BiOI membranes, and TOC removal curves during PCM degradation in BiOI membranes; (f) Actual and stoichiometric  $H_2O_2$  consumptions and the utilization efficiency of  $H_2O_2$  during Fenton-like process in BI-001 membrane; (g) Effect of initial pH on PCM degradation (adjusting pH by 0.1 mM NaOH and HCl); (h) The inactivation efficiency of *E. coli* K-12 and *S. sp.* BM1-1 in the presence of BI-001 and BI-110 membranes. Experimental conditions: [PCM] = 10.0 mg L<sup>-1</sup>, [catalysts loading] = 10.0 mg (except for Fig. 3b), [ $H_2O_2$ ] = 2.0 mM (except for Fig. 3f), initial pH ~5.7 (except for Fig. 3g), T = 25 °C.

enhanced the reaction efficiency between  $H_2O_2$  and the activator, thereby producing a high concentration of ROS. In addition, the limited nanofluid in the BiOI hierarchical structure space shows low mass transfer resistance, boosting the oxidation reaction between target pollutants and the instantaneous free radicals (ultra-short lifetime  $10^{-6}$ – $10^{-9}$  s). When the initial solution passes through the membrane active layer, the contaminants in the initial solution are confined near the surface of the catalyst and the concentration of short-lived free radicals at the membrane interface is significantly higher than that in the static experiment [31]. The estimation of the membrane retention time is given in Fig. S9. In this system, the time for the water to enter the active layer of the membrane is only 10 s, which is much faster than the traditional AOPs. The results of EPR measurement (Fig. S14) conducted using 5,5-dimethyl-pyrroline-oxide (DMPO) as a spin trapping agent confirm that  $\bullet OH$  is the main reactive species [32,33]. The EPR signals in the permeation of BI-110 membrane were much stronger than those obtained from the batch experiments in a high concentration of BI-110 catalyst suspension (0.20 g L<sup>-1</sup>). Moreover, the first-order rate

constant of PCM degradation by BI-110 membrane (Fig. S15) was calculated to be 0.04 s<sup>-1</sup>, approximately 5 times higher than that obtained from the batch suspension reaction ( $8.41 \times 10^{-3}$  s<sup>-1</sup> at pH 5.5). The results indicate that an efficient heterogeneous Fenton-like reaction is driven by BI-110 membrane.

To further verify the hypothesis that the spatial nanoconfinement enhances the kinetics, we synthesized another set of BI-110 loaded membranes using anodized aluminum oxide (AAO) as the template instead of PVDF (Fig. S16). Considering the pore size of PVDF membrane is about 220 nm (see Text S4), thus, the different inner diameters of AAO template with 40–70 nm, 110–150 nm and 200–300 nm was selected to provide different uniform distributed channels, and then BI-110 was immobilized in AAO template membrane to prepare BI-110/AAO<sub>40–70</sub>, BI-110/AAO<sub>110–150</sub> and BI-110/AAO<sub>200–300</sub>. It is observed that the rate constant of BI-110/AAO<sub>200–300</sub> ( $k_{obs} = 0.138$  s<sup>-1</sup>) was much higher than that of BI-110/AAO<sub>110–150</sub> ( $k_{obs} = 0.033$  s<sup>-1</sup>) and BI-110/AAO<sub>40–70</sub> ( $k_{obs} = 0.013$  s<sup>-1</sup>) (Fig. S16a and S16b). The decreased degradation rate of BI-110/AAO<sub>110–150</sub> and BI-110/AAO<sub>40–70</sub> is due to the fact that BI-110

nanocatalyst is difficult to be embedded into the small pores of AAO<sub>40-70</sub> and AAO<sub>110-150</sub>, but was loaded on the surface of AAO pores. In addition, compared with batch reaction of suspended BI-110, BI-110/PVDF also improved the kinetics to a large extent, it is reasonable to propose that the nanoconfinement contributes to the improved exposure of •OH compared with BI-110 suspension.

The curves of the actual and stoichiometric consumption of H<sub>2</sub>O<sub>2</sub> in the BI-110 membrane/H<sub>2</sub>O<sub>2</sub> system as well as the corresponding H<sub>2</sub>O<sub>2</sub> utilization efficiency are shown in Fig. 3f and Table S3, respectively. The appropriate amount of H<sub>2</sub>O<sub>2</sub> was continuously supplied using H<sub>2</sub>O<sub>2</sub> syringe pump to maintain at concentration of ~2 mM in the system (Fig. S17 and S18). In the first 20 s, the actual consumption of H<sub>2</sub>O<sub>2</sub> was very close to its stoichiometric consumption. Before PCM disappears completely, the utilization efficiency of H<sub>2</sub>O<sub>2</sub> reaches more than 66% in the BI-110 membrane/H<sub>2</sub>O<sub>2</sub> system, whereas the H<sub>2</sub>O<sub>2</sub> utilization efficiency in the BI-001 membrane/H<sub>2</sub>O<sub>2</sub> system is only 35% (Fig. S19 and S20). However, the utilization efficiency of H<sub>2</sub>O<sub>2</sub> in the BiOI membrane/H<sub>2</sub>O<sub>2</sub> system is much higher than that of the traditional Fe<sub>3</sub>O<sub>4</sub> (~5%) and Cu<sub>2</sub>O (~20%) Fenton-like systems [33].

By increasing PCM concentration, the degradation efficiency of PCM continues decreasing, which is due to the reaction time within the membrane pores is not adequate to cope with the increasing number of PCM molecules (Fig. S21). The result in Fig. 3g demonstrates that the BiOI membrane/H<sub>2</sub>O<sub>2</sub> system shows the great PCM degradation performance under the initial pH conditions. According to the Zeta potential (Fig. 2f), the isoelectric point value of BI-110 at 25 °C is about 7.30. When the pH of the initial solution is less than the isoelectric point, BI-110 will combine with H<sup>+</sup> via ionization and shows a positively charged surface. In this way, the free radicals will be attractively adsorbed on the surface of the BI-110 membrane through electrostatic interaction, which is beneficial to the oxidative degradation of PCM. However, when the initial pH is adjusted to 2.0, only 18.56% of PCM can be removed within 60 s, which might be attributed to the presence of excessive H<sup>+</sup> hindering the effective contact between H<sub>2</sub>O<sub>2</sub> and the BiOI membrane [35].

*Escherichia coli* K-12 (*E. coli* K-12) and chlorination-resistant *Spingopyxis* sp. BM1-1 (*S. sp.* BM1-1), two common types of waterborne bacteria, were chosen as representative microorganisms to evaluate the

facet-dependent catalytic inactivation activities of BI-001 and BI-110 membranes [36]. In the control experiments, the bacterial population remains unchanged even after 60 s, indicating no toxic effects of BI-001 and BI-110 membranes on bacterial cells (Fig. 3h and Text S10) [37]. Surprisingly, the BI-110 membrane/H<sub>2</sub>O<sub>2</sub> is quite effective in inactivating the bacterial cells, which achieve 6.7 log<sub>10</sub> cfu mL<sup>-1</sup> of *E. coli* K-12 within 40 s and 7.1 log<sub>10</sub> cfu mL<sup>-1</sup> of *S. sp.* BM1-1 within 20 s. However, only 1.4 log<sub>10</sub> cfu mL<sup>-1</sup> *E. coli* K-12 and 2.9 log<sub>10</sub> cfu mL<sup>-1</sup> *S. sp.* BM1-1 were inactivated within 60 s by the BI-001 membrane. The results indicate that BI-110 membrane with antibacterial ability could efficiently achieve water purification.

### 3.3. Interfacial reaction mechanism and electron-donating role of pollutants

The charge transfer between H<sub>2</sub>O<sub>2</sub> and BiOI membranes was evaluated by electrochemical analysis. The total mass of the final coating is 0.00102 g and the coating area is 1 × 1 cm<sup>2</sup> for testing CV and LSV. The cyclic voltammetry (CV) curves of BI-110 and BI-001 are displayed in Fig. 4a. The current intensity of the redox curves of BI-110 is significantly higher than that of BI-001, indicating that BI-110 has a higher surface charge. Electrochemical impedance spectrum (EIS) can reflect the charge transfer efficiency of the interface between the material and the reaction system (Fig. 4b). The arc radius of BI-110 in EIS is smaller than that of BI-001, indicating that the interface charge transfer efficiency of BI-110 is higher than that of BI-001. This could be mainly attributed to the higher amount of OVs in BI-110. The current-time curve (*i-t*) results (Fig. 4c) show that when PCM was added at 268 s, the current density of BI-110 and BI-001 showed an obvious peak and the circuit density peak of BI-110 is larger than that of BI-001, indicating that the electrons transfer from PCM to the BI-110/H<sub>2</sub>O<sub>2</sub> complex is easier than that for BI-001/H<sub>2</sub>O<sub>2</sub> complex. The change of current density may be due to the redistribution of the electron density during the reaction between the catalyst and H<sub>2</sub>O<sub>2</sub> [38]. The linear sweep voltammetry (LSV) results (Fig. 4d) show that the current density increased significantly with the addition of H<sub>2</sub>O<sub>2</sub>, indicating that H<sub>2</sub>O<sub>2</sub> interacted with BI-110 to form a charge transfer (electron donor-acceptor) complex

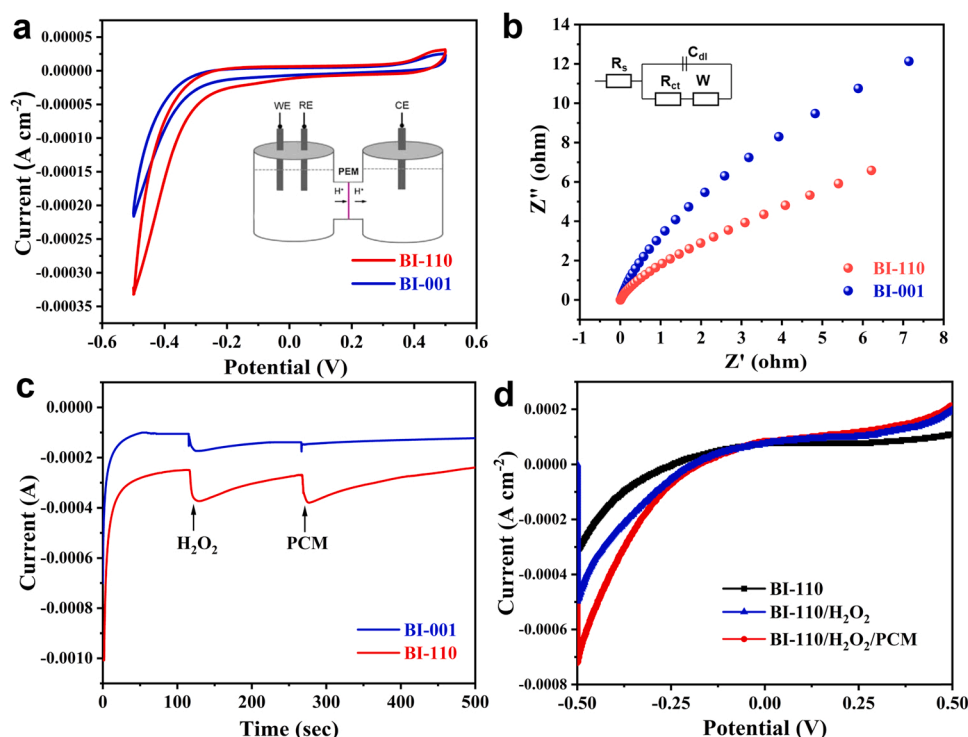


**Fig. 4.** (a) CV curves of BI-110 and BI-001 with a scanning rate of 10 mV s<sup>-1</sup>; (b) EIS of BI-110 and BI-001 in 50 mM Na<sub>2</sub>SO<sub>4</sub> solution, with frequency of 10<sup>6</sup> - 0.01 Hz; (c) *i-t* curve of BiOI with H<sub>2</sub>O<sub>2</sub> and PCM addition obtained at 0.00 V vs. Ag/AgCl using 50 mM Na<sub>2</sub>SO<sub>4</sub> as an electrolyte. The inset is equivalent circuit diagram, in which C<sub>dl</sub>, R<sub>s</sub>, R<sub>ct</sub> and W stands for double layer capacitance, solution resistance, charge transfer resistance and Warburg impedance, respectively; (d) LSV curves of BI-110 under different conditions. Experimental conditions: [PCM] = 10.0 mg L<sup>-1</sup>, [H<sub>2</sub>O<sub>2</sub>] = 2.0 mM, [catalysts loadings] = 10.0 mg, initial pH ~5.7, T = 25 °C.

[3,39]. The addition of PCM triggered another increase in the current density, further confirming that an electric flow transited from PCM to BI-110/H<sub>2</sub>O<sub>2</sub> complex [40,41]. When the current was at 0 A, it is still found that the potential was different for three conditions. The different voltages under the three conditions are probably related to the flat band potential of BI-110 in different system. The flat band potential represents the difference between the Fermi level of the semiconductor and the Fermi level of the electrolyte (the redox potential of some electrolytes in solution) [42]. Generally, the Fermi level of a semiconductor film equilibrates with the redox couple in solution; however, any accumulation of electrons in the film will present a greater shift to more negative potential. As a result, an increase in flat band potential was observed in BI-110/H<sub>2</sub>O<sub>2</sub>/PCM molecules. This result further indicates that the strong electron transfer occurred between H<sub>2</sub>O<sub>2</sub>, PCM molecules, and the surface of catalysts [3,39–41]. According to the above results, the (110) plane and multi-level layered structure can not only provide abundant active sites for the adsorption of PCM, but also increases the electron transfer efficiency.

The in situ Raman test was performed to investigate the interfacial reaction between BiOI and H<sub>2</sub>O<sub>2</sub> (Fig. 5a). In the absence of H<sub>2</sub>O<sub>2</sub>, an obvious peak at 150.5 cm<sup>-1</sup> was observed, which is the characteristic peak of BiOI reflecting the Bi-I stretching vibration of E<sub>g</sub> vibration mode. After adding H<sub>2</sub>O<sub>2</sub>, a strong new peak appeared at 875 cm<sup>-1</sup> representing the adsorption peak of H<sub>2</sub>O<sub>2</sub> onto the surface of catalyst and reflecting the O-O bond vibration of peroxy complexes [43]. This implies that H<sub>2</sub>O<sub>2</sub> combines with the active sites on the surface of BiOI to form a transient complex [44]. With the prolongation of the reaction time, the peak at 875 cm<sup>-1</sup> gradually weakened indicating that H<sub>2</sub>O<sub>2</sub> adsorbed on the active sites was continuously activated and dissociated. Thus, BiOI has a strong chemical adsorption and activation effect on H<sub>2</sub>O<sub>2</sub>. An in situ FTIR spectroscopy analysis was performed to study the adsorption of PCM on the reaction sites of BiOI membrane (Fig. 5b) [45]. For the PCM compound, the band at 3662 cm<sup>-1</sup> corresponds to the O-H stretching vibration of H<sub>2</sub>O, and the broad absorption band near 3400 cm<sup>-1</sup> is attributed to  $\delta_s$  (N-H) amide [46]. In addition, the bands at 2988 and 2901 cm<sup>-1</sup> are ascribed to the stretching vibration of -CH<sub>3</sub>, and the

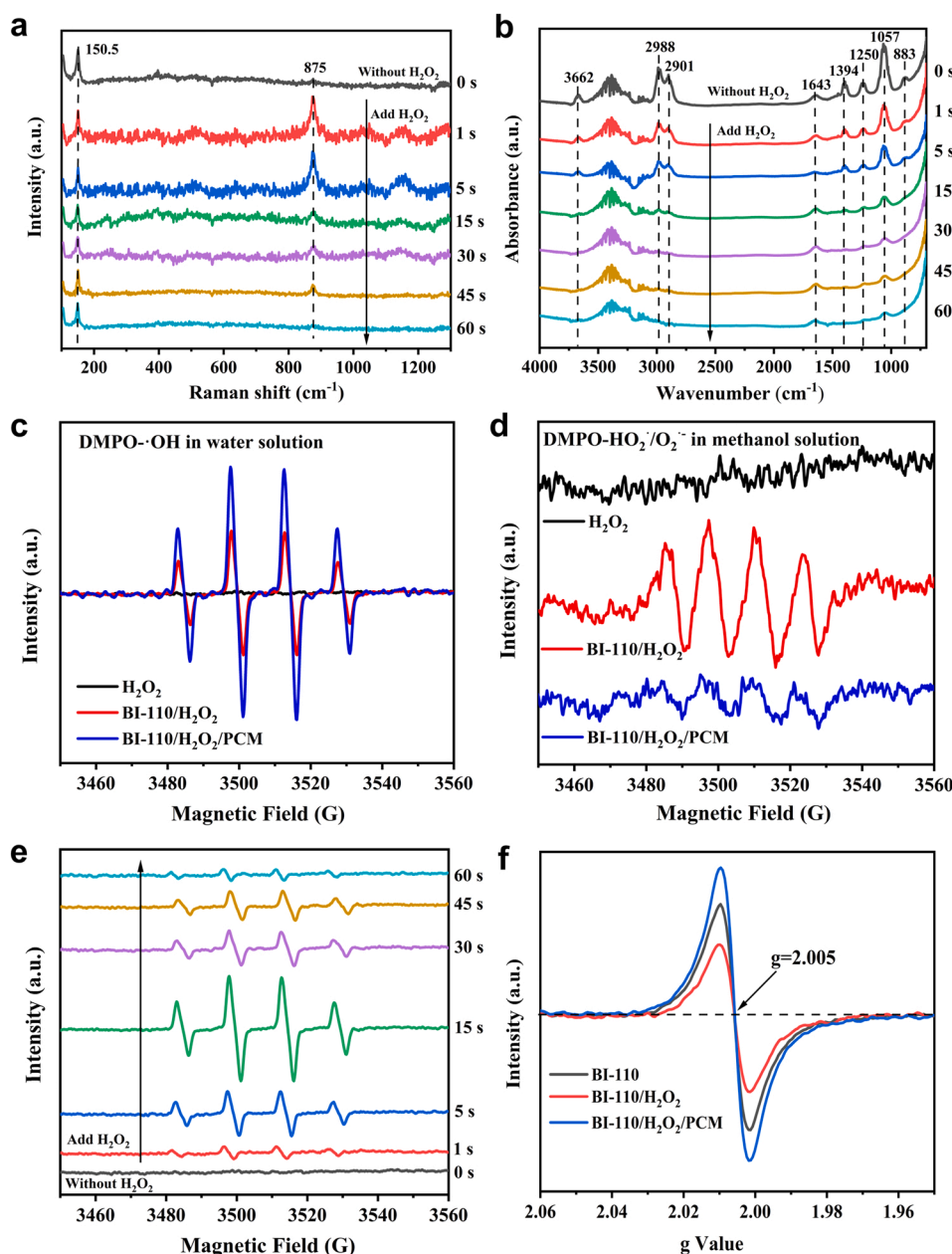


**Fig. 5.** (a) *In situ* Raman spectra of BiOI in aqueous suspensions; (b) *In situ* FTIR for PCM degradation by BI-110 membrane; DMPO spin-trapping EPR spectra for (c) •OH and (d) HO<sub>2</sub>•/O<sub>2</sub>•⁻ in BI-110 membrane in presence of H<sub>2</sub>O<sub>2</sub> with/without pollutants; (e) DMPO spin-trapping EPR spectra for •OH with reaction time in the BI-110 membrane/H<sub>2</sub>O<sub>2</sub> system; (f) Solid EPR spectra of BI-110 membrane before/after reaction in different system. Experimental conditions: [PCM] = 10.0 mg L<sup>-1</sup>, [H<sub>2</sub>O<sub>2</sub>] = 2.0 mM, [catalysts loading] = 10.0 mg, [DMPO] = 200.0 mM (c, d, e), initial pH ~5.7, T = 25 °C.



bands at 883, 1394 and  $1643\text{ cm}^{-1}$  are assigned to the skeleton vibration of the aromatic ring [47]. The band in the range of  $1057\text{--}1250\text{ cm}^{-1}$  corresponds to the C-O stretching vibration in phenol C-OH [48]. After the 60 s, several peaks are gradually reduced and disappeared, indicating that the gradual degradation of PCM.

### 3.4. Conversion of $\text{H}_2\text{O}_2$ on facet-engineered BiOI membrane

The activation of  $\text{H}_2\text{O}_2$  usually includes the generation of ROS. As shown in Fig. S22, PCM removal efficiency was inhibited by 73% after 60 min, while PCM removal efficiency was inhibited by 25% in addition of p-BQ, indicating that the main contribution of  $\bullet\text{OH}$  and  $\text{O}_2^{\bullet-}$  to the whole catalytic reaction. Moreover, the existence of  $\text{K}_2\text{Cr}_2\text{O}_7$  almost completely inhibited the catalytic oxidation of PCM (Fig. S22), thus revealing electron transfer as the main pathway for the generation of active species in Bi-110/ $\text{H}_2\text{O}_2$  system [49,50]. We used DMPO-EPR spectroscopy to detect the  $\text{HO}_2^{\bullet}/\text{O}_2^{\bullet-}$  radicals in methanol solution without  $\text{H}_2\text{O}_2$  [51]. When the Bi-110 was suspended in methanol (Fig. S23), six characteristic peaks of  $\text{DMPO}\cdot\text{HO}_2^{\bullet}/\text{O}_2^{\bullet-}$  were observed, indicating that electron-rich Bi-110 could effectively reduce dissolved  $\text{O}_2$  to  $\text{HO}_2^{\bullet}/\text{O}_2^{\bullet-}$  with abundant electrons as the center. The results show that the Bi-110 transfers an electron from its own electron-rich reactive center to the dissolved  $\text{O}_2$  to generate  $\text{HO}_2^{\bullet}/\text{O}_2^{\bullet-}$ . Therefore, the migration of electron on the surface of Bi-110 membrane is proved. Four characteristic peaks of  $\text{HO}_2^{\bullet}/\text{O}_2^{\bullet-}$  were observed in the Bi-110 membrane/ $\text{H}_2\text{O}_2$  system (Fig. 5d). The abundant  $\text{HO}_2^{\bullet}/\text{O}_2^{\bullet-}$  could be produced by three pathways: (1) the reduction of dissolved  $\text{O}_2$  by the electron-rich reactive centers; (2) the oxidation of  $\text{H}_2\text{O}_2$  by the electron-poor reactive centers; (3) the activation of  $\text{H}_2\text{O}_2$  by of the leached  $\text{Bi}^{3+}$  on the surface of the Bi-110 [15,52,53]. These phenomena indicate that the mutual cooperation of dual reactive centers on the surface of Bi-110 membrane can effectively activate  $\text{H}_2\text{O}_2$  and generate ROS. ESR spectroscopy was further used to detect the generation of free radicals during  $\text{H}_2\text{O}_2$  activation [54]. As shown in Fig. 5c, no signal was detected in the pure  $\text{H}_2\text{O}_2$  system. Four equally spaced (4.4 G) strong peaks with an intensity ratio of 1:2:2:1 were observed in the Bi-110 membrane/ $\text{H}_2\text{O}_2$  system, which was attributed to the signal of 5,5-dimethyl-pyrroline-N-oxide (DMPO)•OH. Especially, the signal intensity is significantly higher than that of Bi-001 membrane/ $\text{H}_2\text{O}_2$  (Fig. S24). This result shows that  $\text{H}_2\text{O}_2$  can rapidly capture single electrons in electron-rich OV and then reduced to  $\bullet\text{OH}$  [55]. Similarly, the signals of  $\text{DMPO}\cdot\text{HO}_2^{\bullet}/\text{O}_2^{\bullet-}$  (four consecutive peaks of the same intensity) were also detected in the Bi-110 membrane/ $\text{H}_2\text{O}_2$  system (Fig. 5d), indicating that  $\text{H}_2\text{O}_2$  was reduced, which was achieved through electron-poor  $\text{Bi}^{3+}$  sites in the absence of contaminants. However, the signal strength of  $\text{DMPO}\cdot\text{HO}_2^{\bullet}/\text{O}_2^{\bullet-}$  in the Bi-110 membrane/ $\text{H}_2\text{O}_2$ /PCM system dropped sharply after adding PCM. This result shows that the pollutant can replace  $\text{H}_2\text{O}_2$  as the electron donor after interacting with  $\text{Bi}^{3+}$  sites, thus preferring to produce  $\bullet\text{OH}$  via the reduction of  $\text{H}_2\text{O}_2$  instead of  $\text{HO}_2^{\bullet}/\text{O}_2^{\bullet-}$  via the oxidation of  $\text{H}_2\text{O}_2$  [15,52,53]. The detection result of  $\bullet\text{OH}$  in the Bi-110 membrane/ $\text{H}_2\text{O}_2$ /PCM system clearly confirmed this phenomenon (Fig. 5c), in which the signal intensity of  $\text{DMPO}\cdot\text{OH}$  significantly increased by two times after adding PCM.

The evolution of the  $\text{DMPO}\cdot\text{OH}$  signal along with the reaction time in the Bi-110 membrane/ $\text{H}_2\text{O}_2$ /PCM system is shown in Fig. 5e. With the increase of reaction time, the signal of  $\text{DMPO}\cdot\text{OH}$  first increases and then decreases, because intrinsic factors were involved in the production and consumption of  $\bullet\text{OH}$  during the reaction. At first, the hydroxylation process of the pollutants consumed the most of  $\bullet\text{OH}$ , thus a low concentration of  $\bullet\text{OH}$  was detected at initial 1 s. Then, the intermediate products appeared along with the hydroxylation, which could be adsorbed on the surface of the Bi-110 and supply electrons to the electron-poor  $\text{Bi}^{3+}$  sites. Then, the obtained electrons were quickly transferred to OVs, resulting in producing more  $\bullet\text{OH}$  by the reduction of  $\text{H}_2\text{O}_2$ . Therefore, the detected  $\text{DMPO}\cdot\text{OH}$  signal increases within the first 15 s. After that, the intermediate hydroxylation products were

gradually degraded and  $\text{H}_2\text{O}_2$  was gradually consumed during the reaction. Therefore, almost no  $\bullet\text{OH}$  was detected at 60 s

To elucidate the surficial reaction processes, the status of the electrons occupied in of OVs on the surface of Bi-110 membrane before and after the reaction were studied by solid EPR spectroscopy. As shown in Fig. 5f and Fig. S25, the EPR signal of OVs on fresh Bi-110 membrane is very strong. After reacting with  $\text{H}_2\text{O}_2$ , the signal intensity dropped sharply, confirming the rapid diffusion of electrons from OVs to  $\text{H}_2\text{O}_2$ . However, the EPR signal of OVs was enhanced with the subsequent addition of PCM, confirming the mechanism of PCM providing electrons for  $\text{H}_2\text{O}_2$  activation. Compared with the fresh Bi-110 membrane, the content of OVs in the Bi-110 membrane obviously decreases to 58% after three cycles of the reaction. This could be explained by the following reasons: The intermediate products in the reaction process covered the surface of the Bi-110 or the highly oxidizing environment changes the chemistry properties of the surface of Bi-110; The active free radicals generated by the activation of  $\text{H}_2\text{O}_2$  could also inactivate a few active sites, leading to a reduction in the number of active sites. Based on the above discussion, the mechanism of  $\text{H}_2\text{O}_2$  activation and pollutant conversion on the surface of BiOI is illustrated as shown in Graphical abstract. The pollutants (hydroxylation product) provide electrons to the electron-poor  $\text{Bi}^{3+}$  sites, and then the electrons diffuse to OVs to activate  $\text{H}_2\text{O}_2$ , maintaining the balance of electron gain and loss in the entire system. Besides, a few  $\text{H}_2\text{O}_2$  can also be oxidized to  $\text{HO}_2^{\bullet}/\text{O}_2^{\bullet-}$  by the valid  $\text{Bi}^{3+}$  sites.

### 3.5. DFT calculations for electronic properties of facet-engineered BiOI membrane

To further verify the polarization adsorption sites of  $\text{H}_2\text{O}_2$  and pollutants, we modulated the adsorption process of  $\text{H}_2\text{O}_2$  and PCM onto the surface sites of BiOI (Fig. S26 and S27). Both the formation energy of OVs ( $E_{\text{vac}}$ ) and adsorption energy ( $E_{\text{ad}}$ ) on the BiOI surface were calculated through DFT calculations (Table S4). The (110) crystal plane of BiOI-110 is a surface with O atoms as the exposed terminal (Fig. 6a, b), and the oxygen atoms can escape from the crystal lattice to form OVs in the original position ( $\Delta E_{\text{vac}}$  (Bi-110) =  $-0.40\text{ eV}$ ). The (001) crystal plane of BiOI-001 has a structure of the open channel (Fig. 6c, d), and the exposed Bi atoms are in a highly unsaturated coordination state ( $\Delta E_{\text{vac}}$  (Bi-001) =  $-1.38\text{ eV}$ ). Therefore, the Bi-O bond is relatively tight and not easy to break, which is not conducive to the formation of OVs. Based on the above discussion, Bi-110 is more prone to form OVs on its surface. Due to the existence of unpaired local electrons, the electron density of OVs is relatively high, forming electron-rich active centers. Thus,  $\text{H}_2\text{O}_2$  was chemically adsorbed in OVs and further produced abundant ROS. The DFT total energy ( $E_{\text{DFT}}$ ) and  $E_{\text{ad}}$  for  $\text{H}_2\text{O}_2$  at the three sites (Bi, OV and I site) are shown in Table S4. Obviously,  $\text{H}_2\text{O}_2$  has the largest negative adsorption energy ( $-1.52\text{ eV}$ ) onto the OVs, indicating that the adsorption of  $\text{H}_2\text{O}_2$  is most stable at this site. This result demonstrates theoretically that  $\text{H}_2\text{O}_2$  does tend to combine with the electron-rich OVs to undergo a reduction reaction. As shown in Fig. 6i, k, the  $E_{\text{ad}}$  of  $\text{H}_2\text{O}_2$  onto the OVs in Bi-110 ( $E_{\text{ad}}$  =  $-1.52\text{ eV}$ ) and Bi-001 ( $E_{\text{ad}}$  =  $-0.89\text{ eV}$ ) are higher than pristine Bi-110 ( $E_{\text{ad}}$  =  $-0.78\text{ eV}$ ) and Bi-001 ( $E_{\text{ad}}$  =  $-0.64\text{ eV}$ ), respectively. Apparently, the OVs in BiOI provides a more stable adsorption site for  $\text{H}_2\text{O}_2$  than pristine BiOI, which could be attributed to the more favorable bond lengths and net atomic charges. This result illustrates that  $\text{H}_2\text{O}_2$  does tend to combine with the electron-rich OVs to undergo a reduction reaction in a Fenton-like process. To reveal the adsorption characteristics of pollutant molecules, DFT calculations for the adsorption of PCM on the surface of BiOI were also performed (Fig. 6j, l). Differently, the negative value in the adsorption energy of PCM onto  $\text{Bi}^{3+}$  sites was found (Table S4). Besides, PCM was preferentially adsorbed onto the Bi-110 ( $E_{\text{ad}}$  =  $-1.05\text{ eV}$ ) than Bi-001 ( $E_{\text{ad}}$  =  $-0.74\text{ eV}$ ). These results theoretically prove that PCM prefers to react with electron-poor  $\text{Bi}^{3+}$  sites by providing electrons and the electron-rich OVs are responsible for capturing  $\text{H}_2\text{O}_2$  to generate

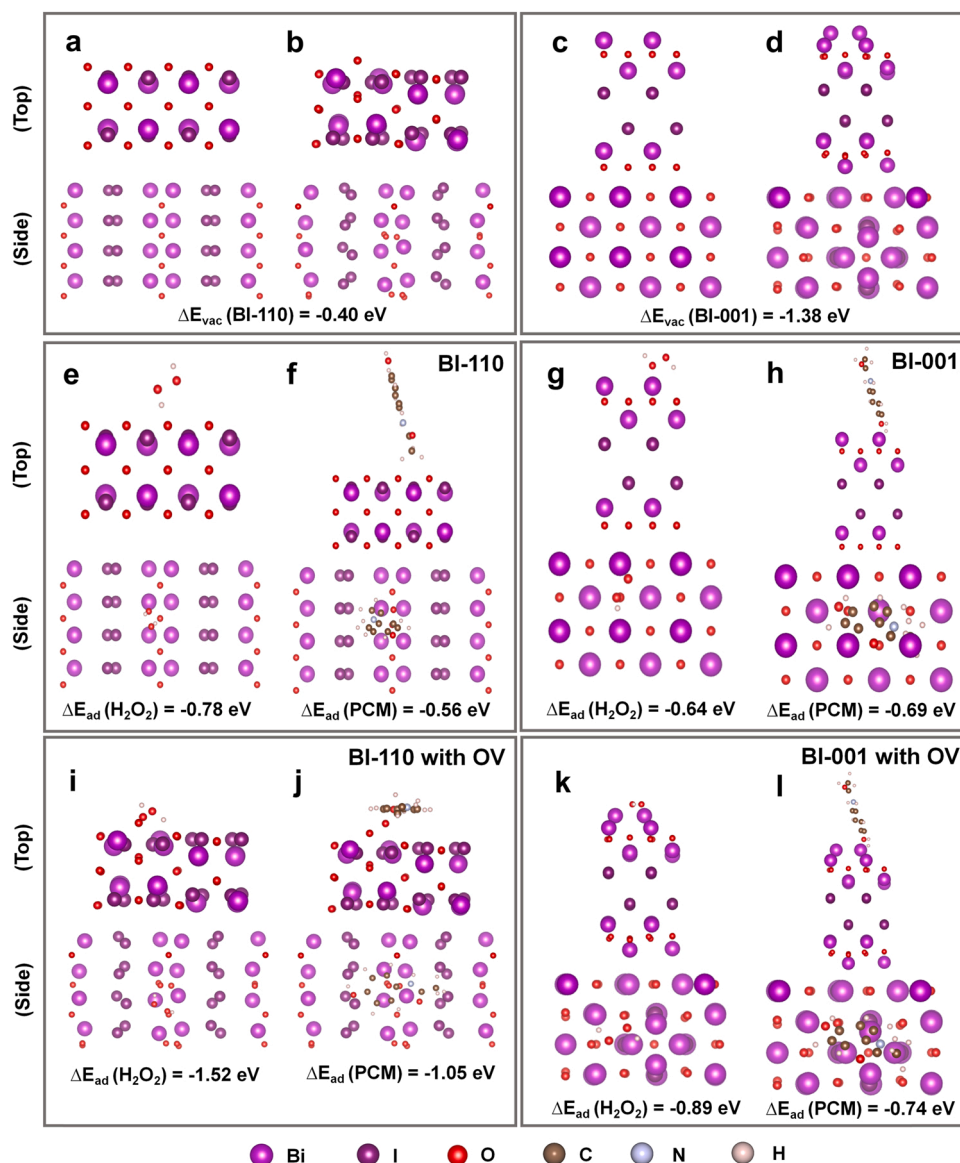


Fig. 6. Atomic configuration of (a) BI-110 and (b) BI-110 with OVs; Atomic configuration of (c) BI-001 and (d) BI-001 with OVs; Top (upper) and side (lower) of optimized adsorption geometries of  $\text{H}_2\text{O}_2$  and PCM on surface of (e, f) pristine BI-110 and (g, h) pristine BI-001, (i, j) BI-110 with OVs and (k, l) BI-001 with OVs.

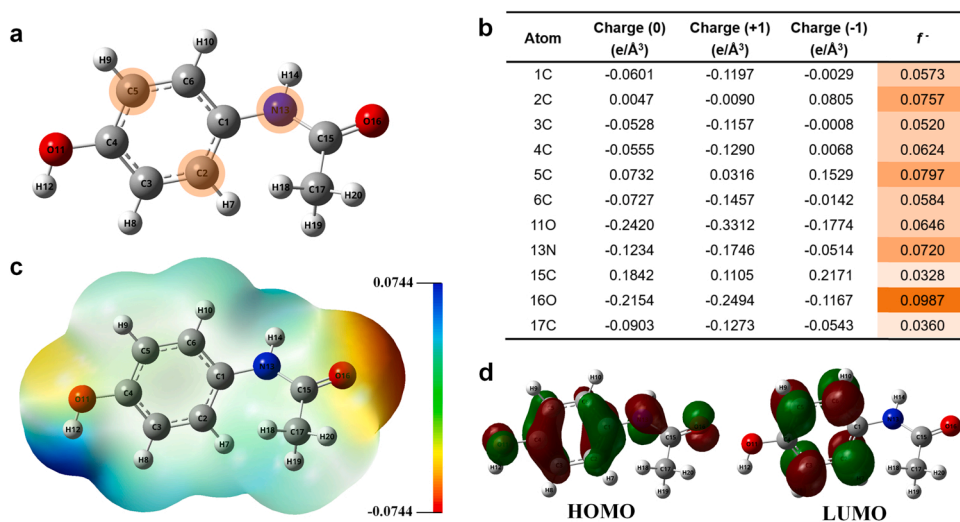


Fig. 7. Natural bond orbital (NBO) analysis for PCM molecule at B3LYP/6-31 +G(d) level. (a) Optimized structure of PCM and numbering system (gray: carbon; red: oxygen; blue: nitrogen; white: hydrogen); (b) Natural population analysis (NPA) charge populations and condensed Fukui index distribution for electrophilic attack (*f*<sup>-</sup>); (c) Electrostatic potential (ESP)-mapped molecular surface of PCM; (d) The highest occupied molecular orbital (HOMO) and the lowest unoccupied molecular orbital (LUMO).

•OH. Therefore, the chemical reactivity of BiOI is significantly enhanced by the formation of the dual reactive centers (electron-rich and electron-poor centers).

### 3.6. Degradation pathways of typical organic pollutants

In order to understand the degradation mechanism of PCM in the BiOI membrane/H<sub>2</sub>O<sub>2</sub> system, Fukui function calculations were performed. The Fukui function is a real-space function commonly used to predict nucleophilic, electrophilic and free radical reaction sites [56]. The optimized PCM model is shown in Fig. 7a. The obtained  $f^+$  value of Fukui function (used to predict the sensitivity of •OH to electrophilically attack PCM molecules) are listed in Fig. 7b. The results show that 13 N ( $f^+ = 0.0720$ ), 4 C ( $f^+ = 0.0624$ ), 16 O ( $f^+ = 0.0987$ ), 2 C ( $f^+ = 0.0757$ ) and 5 C ( $f^+ = 0.0797$ ) are inclined to be electrophilically attacked. However, 11 O and 4 C are saturated sites that cannot accept free radical addition. Therefore, 13 N, 2 C, and 5 C are the most likely sites to be attacked by •OH. Considering the simultaneous occurrence of free radical attack and electrophilic attack, the degradation of PCM could be involved in the various pathways. In addition, the distribution of electrostatic potential and charge can provide useful information for the analysis of the reactive centers. The negatively charged and the positively charged region could be the active sites for reduction and oxidation reactions, respectively. Therefore, we also studied the electrostatic potential (ESP) distribution of PCM (Fig. 7c, d) and the distribution maps with different colors are used to indicate different values of ESP. The red and blue represent the most negative (electron-rich) and most positive (electron-poor) regions, indicating that 13 N with negative ESP is susceptible to be electrophilically attacked by •OH.

To clearly clarify the degradation pathway of PCM, the intermediates and products were determined by liquid chromatography/mass spectrometry (LC/MS) [57–59]. The detected compounds are listed in Table S6, the LC/MS chromatograms of the degraded intermediates are shown in Fig. S28 and the spectrum of HPLC mass analysis chart of the main intermediates at different time is shown in Fig. S29. The proposed degradation pathway of PCM is depicted in Fig. 8. The degradation of PCM includes two possible pathways, which are hydroxylation and C–N bond cleavage. Specifically, the attack at 13 N leads to the cleavage of C–N bond (path I: A→B→C→D→E→F), while the attack at 5 C leads to the hydroxylation of PCM (path II: A→G→H→I→J and path III: A→K→L→M→N→O).

A→K→L→M→N→O). In route IV (pathway IV: A→P→Q→R, A→P→S→T or A→P→S→Q→R), PCM forms dimer through amide methyl group dimerization via free radical activation ( $m/z-301$  [M+H]<sup>+</sup>). With the cleavage of the carbonyl groups and the loss of the vinyl groups, the dimer converts into 1,3-diphenylurea ( $m/z-212$  [M+H]<sup>+</sup>), 4,4'-(hydrazino-1,2-diphenylurea), and diphenol ( $m/z-216$  [M+H]<sup>+</sup>) further converting to N-propyl formamide ( $m/z-87$  [M+H]<sup>+</sup>). It should be pointed out that C–N cleavage process (path I: A→B→C→D→E→F) is the main PCM degradation process with the highest 13 N Fukui index and the great contribution of •OH resulted in this pathway. The deep oxidation of PCM by free radicals leads to the mineralization of intermediates to the final production of CO<sub>2</sub> and H<sub>2</sub>O.

### 3.7. Stability and long-term performance of facet-engineered BiOI membrane

The stability is an important factor affecting the practical application of heterogeneous Fenton catalysts; Thus, the stability of the BiOI should be evaluated accordingly. The morphology of the two kinds of BiOI after the reaction are well remained, demonstrating their excellent stability (Fig. S30). The XRD spectra of the used BI-001 and BI-110 membrane, shown in Fig. S31, reveal no new peaks, indicating that the composition of BI-001 and BI-110 membrane did not change after the reaction. The relative content of oxygen in BiOI membrane basically does not change after the reaction (Fig. S32). BI-110 membrane maintained the complete removal of PCM within 24 h (Fig. 9a). When the run time was further prolonged to 100 h, the degradation of PCM in the membrane reactor only suffered a slight reduction to the removal efficiency of 84.33%. As shown in Fig. 9a, the leaching of bismuth decreased from 2.17 mg L<sup>-1</sup> to less than 0.61 mg L<sup>-1</sup> within 5 h of reaction time and 0.20 mg L<sup>-1</sup> within 24 h of reaction time, which is under the permit concentration of < 50 mg L<sup>-1</sup> based on European Union Discharge Standard. While the release of iodide is also under the safe level (< 10 mg L<sup>-1</sup>) [60]. This result shows the high stability of the BI-110 membrane in the Fenton-like AOPs. Besides, we evaluated the influence of released iodide ions on the degradation performance of PCM by adding 1.0 mM KI to the solution before reaction. As shown in Fig. S33, the degradation performance of PCM is almost unchanged with the addition of iodide ions. Therefore, the role of iodide in Fenton-like catalytic degradation of PCM is negligible.

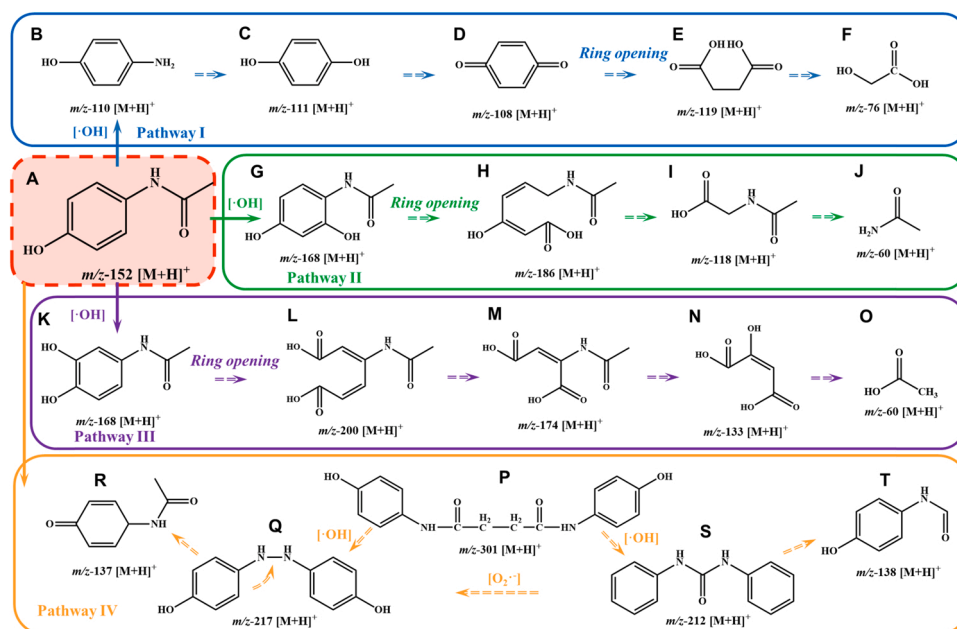
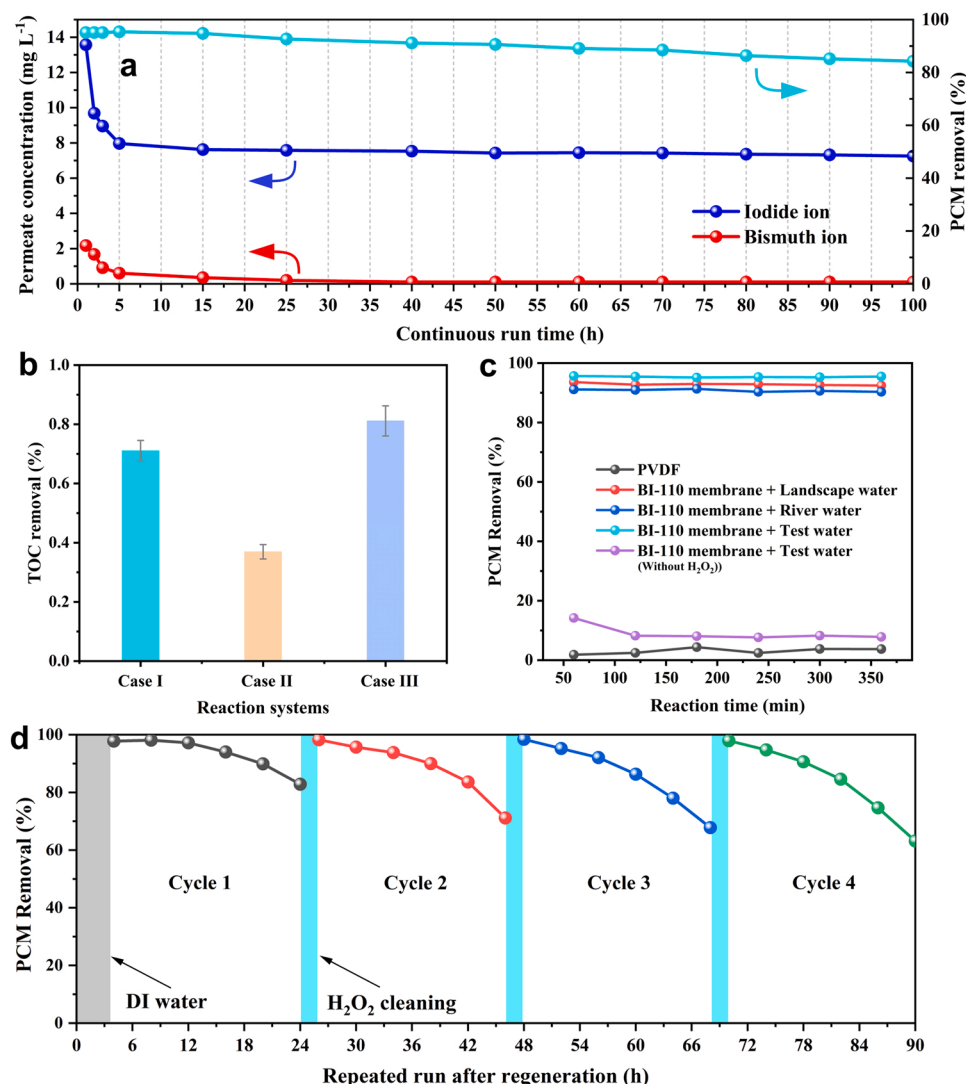


Fig. 8. Proposed degradation pathways of PCM in Bi-110 membrane/H<sub>2</sub>O<sub>2</sub> system.





**Fig. 9.** (a) Permeate concentrations of bismuth and iodide ions versus time for the BI-110 membrane, and removal of PCM during a long-term operation of membrane AOPs; (b) Removal of TOC from the simulated surface water with (test water) and without (NOM only) model pollutants in BI-110 membrane system (Case I: membrane rejection (NOM only); Case II: membrane rejection (test water); Case III: membrane AOP (test water)); (c) Influences of water quality on PCM removal; (d) Decontamination of real water (Table S5 for details), PCM degradation by BI-110 membrane activated H<sub>2</sub>O<sub>2</sub> over four cycles, and water samples were collected every 4 h and immediately sent to analysis. Experimental conditions: [PCM] = 10.0 mg L<sup>-1</sup>, [NOM] = 5 mg L<sup>-1</sup> (Suwannee River NOM), [H<sub>2</sub>O<sub>2</sub>] = 2.0 mM, [catalysts loading] = 10.0 mg, initial pH ~5.7, T = 25 °C.

### 3.8. Performance with the real water matrix of facet-engineered BiOI membrane

We further tested BI-110 membrane using simulated surface water containing common inorganic contaminants and natural organic matter (NOM) spiked with PCM (Table S5). It is well known that NOM can quench •OH and compete with PCM in the degradation process [61]. This phenomenon was also observed in the batch experiments that the NOM (5 mg L<sup>-1</sup>) significantly hindered the degradation of PCM (Fig. S34). However, the use of BI-110 membrane can efficiently solve this issue by eliminating the most of the NOM through size exclusion (~70% in terms of TOC) (Fig. 9b). In other words, the BI-110 resided on the PVDF membrane are not exposed to the majority of NOM, enabling them to selectively remove the PCM with 10 h under an alkalinity of 300 μeq L<sup>-1</sup> (~30 mg L<sup>-1</sup> CaCO<sub>3</sub>) (Fig. S35). Note that for the feed solution containing NOM (5 mg L<sup>-1</sup>) and PCM (10 mg L<sup>-1</sup>), the NOM removal rate of 70% corresponds to the TOC removal ratio of approximately 37% (Fig. 9b, Case II). However, due to the removal of NOM (38%) by size exclusion and the catalytic degradation of PCM (46% in terms of total TOC of feed), the total TOC removal ratio of 82% was achieved.

The influence of background water resources in China, Guangzhou, and spiked with 10 mg L<sup>-1</sup> PCM is illustrated in Fig. 9c. It can be found that the degradation efficiencies of PCM in landscape water and river water (Landscape water from the Center Lake Park in Sun Yat-Sen

University, and river water from the Pearl River in Guangzhou.) were similar and slightly lower than that in test water. The slight decrease might be owing to the interference of the small amounts of anion with the BI-110 membrane. Overall, the BI-110 membrane is still applicable for effective decontamination of PCM in natural water. The practicality was evaluated through several filtration cycles with the BI-110 membrane (Fig. 9d and Table S5). BI-110 membrane completely removed PCM for the first 10 h of continuous filtration, while the removal efficiency gradually decreased for the next 10 h, reaching approximately 82.8% after 20 h. We found that the BI-110 membrane reactivity could be effectively recovered by a successive soaking in H<sub>2</sub>O<sub>2</sub> solution (10 mM) for repeated use. Each cycle includes the filtration of PCM solution for 20 h followed by H<sub>2</sub>O<sub>2</sub> cleaning (10 mM) for 2 h. After the H<sub>2</sub>O<sub>2</sub> soaking, the catalytic activity of the BI-110 membrane was almost totally recovered. Repeated cycles showed a similar pattern of efficient catalytic activity recovery after H<sub>2</sub>O<sub>2</sub> cleaning. The high removal efficiency of PCM by the recovered BI-110 membrane suggests that the catalytic H<sub>2</sub>O<sub>2</sub> cleaning process can efficiently refresh the catalytic activity of the BI-110 membrane. Overall, the BI-110 membrane exhibits excellent stability and reproducibility for water purification.

## 4. Conclusions

This study first proposed the tunable facet-engineered BiOI

membranes for water purification as a dual-reaction-center catalyst. The catalytic performance of BiOI membranes with exposed OV s was investigated. It was confirmed by EPR that the OV s of BiOI can be controlled by crystal plane adjustment. The synthesized BI-110 membrane behaved the great catalytic activity towards the activation of H<sub>2</sub>O<sub>2</sub> and the degradation of PCM, attributing to the electron-rich/poor regions. The spatial nanoconfinement effect enhanced the exposure of •OH, thus triggering the enhanced kinetics in the AOPs. In addition, different from the traditional Fenton-like systems based on the repeated valence changes of the active sites, H<sub>2</sub>O<sub>2</sub> can be oxidized to generate O<sub>2</sub><sup>•−</sup> on the electron-poor Bi sites, and the reduction reaction occurring the electron-rich OV s contributes to the production of •OH. Electrons obtained from the contaminants at electron-poor Bi<sup>3+</sup> sites transferred to electron-rich OV s through an internal “electronic bridge” to achieve a balance of electronic gain/loss. Besides, •OH, the main active oxygen species, enables the BiOI membrane/H<sub>2</sub>O<sub>2</sub> system to selectively react with the specific pollutants with electron-donating groups. Moreover, the relatively low dissolution rate and high removal efficiency during a long-term operation of membrane-confined AOPs indicate the efficient reusability of BiOI membrane. This research expands the scope of H<sub>2</sub>O<sub>2</sub> activators and clarifies the role of electron-rich/poor sites on the membrane-confined AOPs treatment systems to deal with contaminated waters.

### CRedit authorship contribution statement

**Wei Qu:** Investigation, Data curation, Writing – original draft. **Cheng Chen:** Supervision, Writing – review & editing. **Zhuoyun Tang:** Supervision, Writing – review & editing. **Dehua Xia:** Conceptualization, Funding acquisition, Writing – review & editing. **Dingren Ma:** Software, Validation. **Yajing Huang:** Software, Validation. **Qiyu Lian:** Software, Validation. **Chun He:** Conceptualization, Funding acquisition, Writing – review & editing. **Dong Shu:** Visualization, Investigation. **Bin Han:** Visualization, Investigation.

### Declaration of Competing Interest

The authors declare that they have no known competing financial interests or personal relationships that could have appeared to influence the work reported in this paper.

### Acknowledgements

The authors thank the National Natural Science Foundation of China (No. 21876212, 21976214, 41603097, 21673086, 52070195), Science and Technology Research Programs of Guangdong Province (No. 2019A1515011015), the Science and Technology Program of Guangzhou (201904010353), and Fundamental Research Funds for the Central Universities (13lgjc10, 19lgpy157) for financially supporting this work. Dr. Xia was also supported by the Start-up Funds for High-Level Talents of Sun Yat-sen University (38000-18821111). HAADF-STEM-EDS measurements were performed at the Pico Center at Southern University of Science and Technology, which was sponsored by the Presidential Fund and Development and Reform Commission of Shenzhen Municipality.

### Appendix A. Supporting information

Supplementary data associated with this article can be found in the online version at [doi:10.1016/j.apcatb.2021.120970](https://doi.org/10.1016/j.apcatb.2021.120970).

### References

- [1] X.J. Yang, X.M. Xu, J. Xu, Y.F. Han, Iron oxychloride (FeOCl): an efficient Fenton-like catalyst for producing hydroxyl radicals in degradation of organic contaminants, *J. Am. Chem. Soc.* 135 (2013) 16058–16061, <https://doi.org/10.1021/ja409130c>.
- [2] M. Xie, F. Dai, J. Li, X. Dang, J. Guo, W. Lv, Z. Zhang, X. Lu, Tailoring the electronic metal-support interactions in supported atomically dispersed gold catalysts for efficient Fenton-like reaction, *Angew. Chem. Int. Ed.* 60 (2021) 14370–14375, <https://doi.org/10.1002/anie.202103652>.
- [3] C. Chen, T. Ma, Y. Shang, B. Gao, B. Jin, H. Dan, Q. Li, Q. Yue, Y. Li, Y. Wang, X. Xu, In-situ pyrolysis of Enteromorpha as carbocatalyst for catalytic removal of organic contaminants: considering the intrinsic N/Fe in Enteromorpha and non-radical reaction, *Appl. Catal. B: Environ.* 250 (2019) 382–395, <https://doi.org/10.1016/j.apcatb.2019.03.048>.
- [4] D.B. Miklos, C. Remy, M. Jekel, K.G. Linden, J.E. Drewes, U. Hubner, Evaluation of advanced oxidation processes for water and wastewater treatment - a critical review, *Water Res.* 139 (2018) 118–131, <https://doi.org/10.1016/j.watres.2018.03.042>.
- [5] X. Cui, W. Li, P. Ryabchuk, K. Junge, M. Beller, Bridging homogeneous and heterogeneous catalysis by heterogeneous single-metal-site catalysts, *Nat. Catal.* 1 (2018) 385–397, <https://doi.org/10.1038/s41929-018-0090-9>.
- [6] Y. Zhu, R. Zhu, Y. Xi, J. Zhu, G. Zhu, H. He, Strategies for enhancing the heterogeneous Fenton catalytic reactivity: a review, *Appl. Catal. B: Environ.* 255 (2019), 117739, <https://doi.org/10.1016/j.apcatb.2019.05.041>.
- [7] D. Xia, H. He, H. Liu, Y. Wang, Q. Zhang, Y. Li, A. Lu, C. He, P.K. Wong, Persulfate-mediated catalytic and photocatalytic bacterial inactivation by magnetic natural ilmenite, *Appl. Catal. B: Environ.* 238 (2018) 70–81, <https://doi.org/10.1016/j.apcatb.2018.07.003>.
- [8] L. Zhu, J. Ji, J. Liu, S. Mine, M. Matsuoka, J. Zhang, M. Xing, Designing 3D-MoS<sub>2</sub> sponge as excellent cocatalysts in advanced oxidation processes for pollutant control, *Angew. Chem. Int. Ed.* 59 (2020) 13968–13976, <https://doi.org/10.1002/anie.202006059>.
- [9] L. Lyu, L. Zhang, G. He, H. He, C. Hu, Selective H<sub>2</sub>O<sub>2</sub> conversion to hydroxyl radicals in the electron-rich area of hydroxylated C-g-C<sub>3</sub>N<sub>4</sub>/CuCo-Al<sub>2</sub>O<sub>3</sub>, *J. Mater. Chem. A* 5 (2017) 7153–7164, <https://doi.org/10.1039/c7ta01583f>.
- [10] J. Ma, L. Xu, C. Shen, C. Hu, W. Liu, Y. Wen, Fe-N-Graphene wrapped Al<sub>2</sub>O<sub>3</sub>/pentlandite from microalgae: high fenton catalytic efficiency from enhanced Fe<sup>3+</sup>-reduction, *Environ. Sci. Technol.* 52 (2018) 3608–3614, <https://doi.org/10.1021/acs.est.7b03412>.
- [11] S. Xu, H. Zhu, W. Cao, Z. Wen, J. Wang, C.P. François-Xavier, T. Wintgens, Cu-Al<sub>2</sub>O<sub>3</sub>-g-C<sub>3</sub>N<sub>4</sub> and Cu-Al<sub>2</sub>O<sub>3</sub>-C-dots with dual-reaction centres for simultaneous enhancement of Fenton-like catalytic activity and selective H<sub>2</sub>O<sub>2</sub> conversion to hydroxyl radicals, *Appl. Catal. B: Environ.* 234 (2018) 223–233, <https://doi.org/10.1016/j.apcatb.2018.04.029>.
- [12] L. Lyu, G. Yu, L. Zhang, C. Hu, Y. Sun, 4-Phenoxyphenol-functionalized reduced graphene oxide nanosheets: a metal-free Fenton-like catalyst for pollutant destruction, *Environ. Sci. Technol.* 52 (2018) 747–756, <https://doi.org/10.1021/acs.est.7b04865>.
- [13] W. Cao, M. Han, L. Lyu, C. Hu, F. Xiao, Efficient Fenton-like process induced by fortified electron-rich O microcenter on the reduction state Cu-doped CNO polymer, *ACS Appl. Mater. Interfaces* 11 (2019) 16496–16505, <https://doi.org/10.1021/acsami.9b00195>.
- [14] P. Gao, X. Chen, M. Hao, F. Xiao, S. Yang, Oxygen vacancy enhancing the Fe<sub>2</sub>O<sub>3</sub>-CeO<sub>2</sub> catalysts in Fenton-like reaction for the sulfamerazine degradation under O<sub>2</sub> atmosphere, *Chemosphere* 228 (2019) 521–527, <https://doi.org/10.1016/j.chemosphere.2019.04.125>.
- [15] H. Li, J. Shang, Z. Yang, W. Shen, Z. Ai, L. Zhang, Oxygen vacancy associated surface Fenton chemistry: Surface structure dependent hydroxyl radicals generation and substrate dependent reactivity, *Environ. Sci. Technol.* 51 (2017) 5685–5694, <https://doi.org/10.1021/acs.est.7b00040>.
- [16] X. Chen, G. Huang, Y. Li, C. An, R. Feng, Y. Wu, J. Shen, Functional PVDF ultrafiltration membrane for Tetrabromobisphenol-A (TBBPA) removal with high water recovery, *Water Res.* 181 (2020), 115952, <https://doi.org/10.1016/j.watres.2020.115952>.
- [17] L. Ni, Y. Zhu, J. Ma, Y. Wang, Novel strategy for membrane biofouling control in MBR with CdS/MIL-101 modified PVDF membrane by in situ visible light irradiation, *Water Res.* 188 (2021), 116554, <https://doi.org/10.1016/j.watres.2020.116554>.
- [18] R.F. Nogueira, M.C. Oliveira, W.C. Paterlini, Simple and fast spectrophotometric determination of H<sub>2</sub>O<sub>2</sub> in photo-Fenton reactions using metavanadate, *Talanta* 66 (2005) 86–91, <https://doi.org/10.1016/j.talanta.2004.10.001>.
- [19] S. Al Aani, V. Gomez, C.J. Wright, N. Hilal, Fabrication of antibacterial mixed matrix nanocomposite membranes using hybrid nanostructure of silver coated multi-walled carbon nanotubes, *Chem. Eng. J.* 326 (2017) 721–736, <https://doi.org/10.1016/j.cej.2017.06.029>.
- [20] W. Qu, H. Zhao, Q. Zhang, D. Xia, Z. Tang, Q. Chen, C. He, D. Shu, Multifunctional Au/Ti<sub>3</sub>C<sub>2</sub> photothermal membrane with antibacterial ability for stable and efficient solar water purification under the full spectrum, *ACS Sustain. Chem. Eng.* 9 (2021) 11372–11387, <https://doi.org/10.1021/acssuschemeng.1c03096>.
- [21] J. Sun, J. Wen, G. Wu, Z. Zhang, X. Chen, G. Wang, M. Liu, Harmonizing the electronic structures on BiOI with active oxygen vacancies toward facet-dependent antibacterial photodynamic therapy, *Adv. Funct. Mater.* 30 (2020), 2004108, <https://doi.org/10.1002/adfm.202004108>.
- [22] L. Hu, Y. Liao, D. Xia, F. Peng, L. Tan, S. Hu, C. Zheng, X. Lu, C. He, D. Shu, Engineered photocatalytic fuel cell with oxygen vacancies-rich rGO/BiOI-xl as photoanode and biomass-derived N-doped carbon as cathode: promotion of reactive oxygen species production via Fe<sup>2+</sup>/Fe<sup>3+</sup> redox, *Chem. Eng. J.* 385 (2020), 123824, <https://doi.org/10.1016/j.cej.2019.123824>.
- [23] C. Wang, H. Hu, S. Yan, Q. Zhang, Activating Bi<sub>2</sub>O<sub>3</sub> by ball milling to induce efficiently oxygen vacancy for incorporating iodide anions to form BiOI, *Chem. Phys.* 533 (2020), 110739, <https://doi.org/10.1016/j.chemphys.2020.110739>.

- [24] Y. Bu, H. Li, W. Yu, Y. Pan, L. Li, Y. Wang, L. Pu, J. Ding, G. Gao, B. Pan, Peroxydisulfate activation and singlet oxygen generation by oxygen vacancy for degradation of contaminants, *Environ. Sci. Technol.* 55 (2021) 2110–2120, <https://doi.org/10.1021/acs.est.0c07274>.
- [25] J. Ding, Z. Dai, F. Tian, B. Zhou, B. Zhao, H. Zhao, Z. Chen, Y. Liu, R. Chen, Generation of defect clusters for  $\text{IO}_2$  production for molecular oxygen activation in photocatalysis, *J. Mater. Chem. A* 5 (2017) 23453–23459, <https://doi.org/10.1039/c7ta08117k>.
- [26] S. Uhlenbrock, C. Scharfschwerdt, M. Neumann, G. Illing, H.J. Freund, The influence of defects on the Ni 2p and O 1s XPS of NiO, *J. Phys.: Condens. Matter* 4 (1992) 7973–7978, <https://doi.org/10.1088/0953-8984/4/40/009>.
- [27] Y. Wang, Y. Long, D. Zhang, Facile in situ growth of high strong BiOI network films on metal wire meshes with photocatalytic activity, *ACS Sustain. Chem. Eng.* 5 (2017) 2454–2462, <https://doi.org/10.1021/acssuschemeng.6b02810>.
- [28] D. Yao, C. Tang, A. Vasileff, X. Zhi, Y. Jiao, S.Z. Qiao, The controllable reconstruction of Bi-MOFs for electrochemical  $\text{CO}_2$  reduction through electrolyte and potential mediation, *Angew. Chem. Int. Ed.* 60 (2021) 18178–18184, <https://doi.org/10.1002/anie.202104747>.
- [29] C. Mao, H. Cheng, H. Tian, H. Li, W.-J. Xiao, H. Xu, J. Zhao, L. Zhang, Visible light driven selective oxidation of amines to imines with BiOCl: Does oxygen vacancy concentration matter? *Appl. Catal. B: Environ.* 228 (2018) 87–96, <https://doi.org/10.1016/j.apcatb.2018.01.018>.
- [30] P. Wang, X. Li, S. Fan, X. Chen, M. Qin, D. Long, M.O. Tade, S. Liu, Impact of oxygen vacancy occupancy on piezo-catalytic activity of BaTiO<sub>3</sub> nanobel, *Appl. Catal. B Environ.* 279 (2020), 119340, <https://doi.org/10.1016/j.apcatb.2020.119340>.
- [31] Y. Chen, G. Zhang, H. Liu, J. Qu, Confining free radicals in close vicinity to contaminants enables ultrafast Fenton-like processes in the interspacing of MoS<sub>2</sub> membranes, *Angew. Chem. Int. Ed.* 58 (2019) 8134–8138, <https://doi.org/10.1002/anie.201903531>.
- [32] Q. Lian, A. Roy, O. Kizilkaya, D.D. Gang, W. Holmes, M.E. Zappi, X. Zhang, H. Yao, Uniform mesoporous amorphous cobalt-inherent silicon oxide as a highly active heterogeneous catalyst in the activation of peroxymonosulfate for rapid oxidation of 2,4-dichlorophenol: The important role of inherent cobalt in the catalytic mechanism, *ACS Appl. Mater. Interfaces* 12 (2020) 57190–57206, <https://doi.org/10.1021/acsami.0c20341>.
- [33] D. Xia, H. Liu, B. Xu, Y. Wang, Y. Liao, Y. Huang, L. Ye, C. He, P.K. Wong, R. Qiu, Single Ag atom engineered 3D-MnO<sub>2</sub> porous hollow microspheres for rapid photothermocatalytic inactivation of *E. coli* under solar light, *Appl. Catal. B Environ.* 245 (2019) 177–189, <https://doi.org/10.1016/j.apcatb.2018.12.056>.
- [35] W. Chen, J. Xie, X. Li, L. Li, Oxygen vacancies and Lewis sites activating O<sub>3</sub>/H<sub>2</sub>O<sub>2</sub> at wide pH range via surface electron transfer over CeO<sub>x</sub>/SiO<sub>2</sub> for nitrobenzene mineralization, *J. Hazard. Mater.* 406 (2021), 124766, <https://doi.org/10.1016/j.jhazmat.2020.124766>.
- [36] D. Xia, I.M.C. Lo, Synthesis of magnetically separable Bi<sub>2</sub>O<sub>4</sub>/Fe<sub>3</sub>O<sub>4</sub> hybrid nanocomposites with enhanced photocatalytic removal of ibuprofen under visible light irradiation, *Water Res.* 100 (2016) 393–404, <https://doi.org/10.1016/j.watres.2016.05.026>.
- [37] D. Xia, Y. Li, G. Huang, R. Yin, T. An, G. Li, H. Zhao, A. Lu, P.K. Wong, Activation of persulfates by natural magnetic pyrrhotite for water disinfection: efficiency, mechanisms, and stability, *Water Res.* 112 (2017) 236–247, <https://doi.org/10.1016/j.watres.2017.01.052>.
- [38] E.-T. Yun, G.-H. Moon, H. Lee, T.H. Jeon, C. Lee, W. Choi, J. Lee, Oxidation of organic pollutants by peroxymonosulfate activated with low-temperature-modified nanodiamonds: Understanding the reaction kinetics and mechanism, *Appl. Catal. B Environ.* 237 (2018) 432–441, <https://doi.org/10.1016/j.apcatb.2018.04.067>.
- [39] Y. Gao, Y. Zhu, L. Lyu, Q. Zeng, X. Xing, C. Hu, Electronic structure modulation of graphitic carbon nitride by oxygen doping for enhanced catalytic degradation of organic pollutants through peroxymonosulfate activation, *Environ. Sci. Technol.* 52 (2018) 14371–14380, <https://doi.org/10.1021/acs.est.8b05246>.
- [40] M. Wang, Y. Cui, H. Cao, P. Wei, C. Chen, X. Li, J. Xu, G. Sheng, Activating peroxydisulfate with Co<sub>3</sub>O<sub>4</sub>/NiCo<sub>2</sub>O<sub>4</sub> double-shelled nanocages to selectively degrade bisphenol A – a nonradical oxidation process, *Appl. Catal. B: Environ.* 282 (2021), 119585, <https://doi.org/10.1016/j.apcatb.2020.119585>.
- [41] S. Zhu, X. Huang, F. Ma, L. Wang, X. Duan, S. Wang, Catalytic removal of aqueous contaminants on N-Doped graphitic biochars: Inherent roles of adsorption and nonradical mechanisms, *Environ. Sci. Technol.* 52 (2018) 8649–8658, <https://doi.org/10.1021/acs.est.8b01817>.
- [42] P. Peljo, H.H. Girault, Electrochemical potential window of battery electrolytes: the HOMO–LUMO misconception, *Energy Environ. Sci.* 11 (2018) 2306–2309, <https://doi.org/10.1039/c8ee01286e>.
- [43] E. Clavijo, J.R. Menéndez, R. Aroca, Vibrational and surface-enhanced Raman spectra of vanillic acid, *J. Raman Spectrosc.* 39 (2008) 1178–1182, <https://doi.org/10.1002/jrs.1959>.
- [44] U.P. Agarwal, R.S. Reiner, Near-IR surface-enhanced Raman spectrum of lignin, *J. Raman Spectrosc.* 40 (2009) 1527–1534, <https://doi.org/10.1002/jrs.2294>.
- [45] J. Yang, Y. Huang, Y.-W. Chen, D. Xia, C.-Y. Mou, L. Hu, J. Zeng, C. He, P.K. Wong, H.-Y. Zhu, Active site-directed tandem catalysis on CuO/VO–MnO<sub>2</sub> for efficient and stable catalytic ozonation of S-VOCs under mild condition, *Nano Today* 35 (2020), 100944, <https://doi.org/10.1016/j.nantod.2020.100944>.
- [46] Y. Mikhaylova, G. Adam, L. Häussler, K.J. Eichhorn, B. Voit, Temperature-dependent FTIR spectroscopic and thermoanalytic studies of hydrogen bonding of hydroxyl (phenolic group) terminated hyperbranched aromatic polyesters, *J. Mol. Struct.* 788 (2006) 80–88, <https://doi.org/10.1016/j.molstruc.2005.11.020>.
- [47] X. Li, X. Dai, J. Takahashi, N. Li, J. Jin, L. Dai, B. Dong, New insight into chemical changes of dissolved organic matter during anaerobic digestion of dewatered sewage sludge using EEM-PARAFAC and two-dimensional FTIR correlation spectroscopy, *Bioresour. Technol.* 159 (2014) 412–420, <https://doi.org/10.1016/j.biortech.2014.02.085>.
- [48] M. Pan, H. Zhang, G. Gao, L. Liu, W. Chen, Facet-dependent catalytic activity of nanosheet-assembled bismuth oxyiodide microspheres in degradation of bisphenol A, *Environ. Sci. Technol.* 49 (2015) 6240–6248, <https://doi.org/10.1021/acs.est.5b00626>.
- [49] D. Xia, W. Xu, Y. Wang, J. Yang, Y. Huang, L. Hu, C. He, D. Shu, D.Y.C. Leung, Z. Pang, Enhanced performance and conversion pathway for catalytic ozonation of methyl mercaptan on single-atom Ag deposited three-dimensional ordered mesoporous MnO<sub>2</sub>, *Environ. Sci. Technol.* 52 (2018) 13399–13409, <https://doi.org/10.1021/acs.est.8b03696>.
- [50] C. He, Y. Wang, Z. Li, Y. Huang, Y. Liao, D. Xia, S. Lee, Facet engineered  $\alpha$ -MnO<sub>2</sub> for efficient catalytic ozonation of odor CH<sub>3</sub>SH: oxygen vacancy-induced active centers and catalytic mechanism, *Environ. Sci. Technol.* 54 (2020) 12771–12783, <https://doi.org/10.1021/acs.est.0c05235>.
- [51] N. Wang, L. Zhu, M. Lei, Y. She, M. Cao, H. Tang, Ligand-induced drastic enhancement of catalytic activity of nano-BiFeO<sub>3</sub> for oxidative degradation of bisphenol A, *ACS Catal.* 1 (2011) 1193–1202, <https://doi.org/10.1021/cs2002862>.
- [52] H. Wang, D. Yong, S. Chen, S. Jiang, X. Zhang, W. Shao, Q. Zhang, W. Yan, B. Pan, Y. Xie, Oxygen-vacancy-mediated exciton dissociation in BiOBr for boosting charge-carrier-involved molecular oxygen activation, *J. Am. Chem. Soc.* 140 (2018) 1760–1766, <https://doi.org/10.1021/jacs.7b10997>.
- [53] L. Wang, D. Yan, L. Lyu, C. Hu, N. Jiang, L. Zhang, Notable light-free catalytic activity for pollutant destruction over flower-like BiOI microspheres by a dual-reaction-center Fenton-like process, *J. Colloid Interface Sci.* 527 (2018) 251–259, <https://doi.org/10.1016/j.jcis.2018.05.055>.
- [54] L. Lyu, L. Zhang, Q. Wang, Y. Nie, C. Hu, Enhanced fenton catalytic efficiency of gamma-Cu–Al<sub>2</sub>O<sub>3</sub> by sigma-Cu<sub>2</sub>–Ligand complexes from aromatic pollutant degradation, *Environ. Sci. Technol.* 49 (2015) 8639–8647, <https://doi.org/10.1021/acs.est.5b00445>.
- [55] X.X. Guo, T.T. Hu, B. Meng, Y. Sun, Y.-F. Han, Catalytic degradation of anthraquinone-containing H<sub>2</sub>O<sub>2</sub> production effluent over layered Co-Cu hydroxides: defects facilitating hydroxyl radicals generation, *Appl. Catal. B: Environ.* 260 (2020), 118157, <https://doi.org/10.1016/j.apcatb.2019.118157>.
- [56] Q. Zhang, W. Huang, Y.B. Yu, Y.L. Zhou, J.M. Hong, Catalytic performance and mechanism of graphene electrode doped with S and N heteroatoms for N-(4-hydroxyphenyl)ethanamide electrochemical degradation, *J. Hazard. Mater.* 368 (2019) 316–325, <https://doi.org/10.1016/j.jhazmat.2019.01.041>.
- [57] F. Fanaei, G. Moussavi, V. Srivastava, M. Sillanpää, The enhanced catalytic potential of sulfur-doped MgO (S-MgO) nanoparticles in activation of peroxydisulfates for advanced oxidation of acetaminophen, *Chem. Eng. J.* 371 (2019) 404–413, <https://doi.org/10.1016/j.cej.2019.04.007>.
- [58] T.W. Tseng, T.W. Chen, S.M. Chen, T. Kokulnathan, F. Ahmed, P.M.Z. Hasan, A. L. Bilgrami, S. Kumar, Construction of strontium phosphate/graphitic-carbon nitride: a flexible and disposable strip for acetaminophen detection, *J. Hazard. Mater.* (2020), 124542, <https://doi.org/10.1016/j.jhazmat.2020.124542>.
- [59] R. Yin, L. Hu, D. Xia, J. Yang, C. He, Y. Liao, Q. Zhang, J. He, Hydroxylamine promoted Fe(III)/Fe(II) cycle on ilmenite surface to enhance persulfate catalytic activation and aqueous pharmaceutical ibuprofen degradation, *Catal. Today* 358 (2020) 294–302, <https://doi.org/10.1016/j.cattod.2019.04.081>.
- [60] J. Xie, Z. Liao, M. Zhang, L. Ni, J. Qi, C. Wang, X. Sun, L. Wang, S. Wang, J. Li, Sequential ultrafiltration-catalysis membrane for excellent removal of multiple pollutants in water, *Environ. Sci. Technol.* 55 (2021) 2652–2661, <https://doi.org/10.1021/acs.est.0c07418>.
- [61] M.E. Lindsey, M.A. Tarr, Inhibition of hydroxyl radical reaction with aromatics by dissolved natural organic matter, *Environ. Sci. Technol.* 34 (2000) 444–449, <https://doi.org/10.1021/es990457c>.